UNIVERSITY OF CALIFORNIA,
IRVINE

Constraining Cosmological Models Using Non-Gaussian Perturbations in the Cosmic Microwave Background

DISSERTATION

submitted in partial satisfaction of the requirements
for the degree of

DOCTOR OF PHILOSOPHY

in Physics

by

Jon-Michael O'Bryan

Dissertation Committee:
Professor Asantha Cooray, Chair
Professor Steven Barwick
Professor Kevork N. Abazajian

2015

DEDICATION

To Jen

TABLE OF CONTENTS

LIST OF FIGURES

LIST OF TABLES

ACKNOWLEDGMENTS

I would like to thank Joseph Smidt, Cameron Thacker, Jae Calanog, Hai Fu, Chang Feng, and Ketron Mitchell-Wynne who have assisted me directly or indirectly with my research over the past 3 years. Their support and encouragement has made this journey enjoyable and has gotten me through many difficult times.

I would like to thank Asantha Cooray, whose group I have been a part of for that time, for graciously hosting me and providing me with research opportunities and insights. Asantha has always insured that I received some of the best mentorship I've ever received by providing his own advice or by connecting me with other qualified physicists.

I would like to especially thank Jennifer Rha who has helped me persist in completing this program.

Asantha's work was supported by NSF CAREER AST-0645427 and NSF CAREER AST-1313319.

CURRICULUM VITAE

Jon-Michael O'Bryan

EDUCATION

Doctor of Philosophy Physics **2015**
University of California, Irvine *Irvine, CA*

Master of Science Physics **2011**
University of California, Irvine *Irvine, CA*

Bachelor of Science in Mathematics and Physics **2010**
Stanford University *Stanford, CA*

RESEARCH EXPERIENCE

Graduate Research Assistant **2010–2015**
University of California, Irvine *Irvine, California*

Undergraduate Summer Research **2009–2010**
SLAC National Accelerator Laborator, Menlo Park *Menlo Park, California*

TEACHING EXPERIENCE

Teaching Assistant **2010–2013**
University of California, Irvine *Irvine, CA*

PUBLICATIONS

Planck Trispectrum Constraints on Primordial Non-Gaussianity at Cubic Order **2015**

Feng, C., Cooray, A., Smidt, J., O'Bryan, J., Keating, B., Regan, D., Phys. Rev. D92, 043509, (2015)

Constraints on Spatial Variations in the Fine-Structure Constant from Planck **2014**

O'Bryan, J., Smidt, J., De Bernardis, F., Cooray, A., Astrophys. J., 798, 118, (2014)

Compatibility of Theta13 and the Type I Seesaw Model with A4 Symmetry **2013**

Chen, M.-C., Huang, J., O'Bryan, J.-M., Wijangco, A., JHEP 1007, 021 (2013)

ABSTRACT OF THE DISSERTATION

Constraining Cosmological Models Using Non-Gaussian Perturbations in the Cosmic Microwave Background

By

Jon-Michael O'Bryan

Doctor of Philosophy in Physics

University of California, Irvine, 2015

Professor Asantha Cooray, Chair

We study non-Gaussian distributions in temperature fluctuations of the cosmic microwave background radiation. We introduce a novel way of measuring spatial variations in the fine-structure constant with these tools. We also lay out the method of measuring the first non-Gaussian moment using the three-point correlation function and an optimized estimator and apply these methods to the Planck CMB maps.

Chapter 1

Introduction

1.1 Cosmic Microwave Background

Shortly after Big Bang, there was a hot, dense fog of particles. Eventually (around 380,000 years after the Big Bang), the temperature dropped sufficiently that electrons coupled with protons to form neutral hydrogen atoms (i.e., recombination). This recombination removed from the fog free electrons which caused photons to scatter through Thomson scattering. Thus, the fog broke enough for photons to travel freely (without being scattered off of other particles). The light that has traveled freely from that point is visible to us. That light is called the Cosmic Microwave Background radiation, or the CMB.

1.1.1 Experiments Detecting the CMB

From the 1940's to the 1960's, physicists favoring a Big Bang theory for the origin of the universe estimated that the radiation coming from the earliest visible times in the universe would have temperatures of somewhere between 5K and 50K.

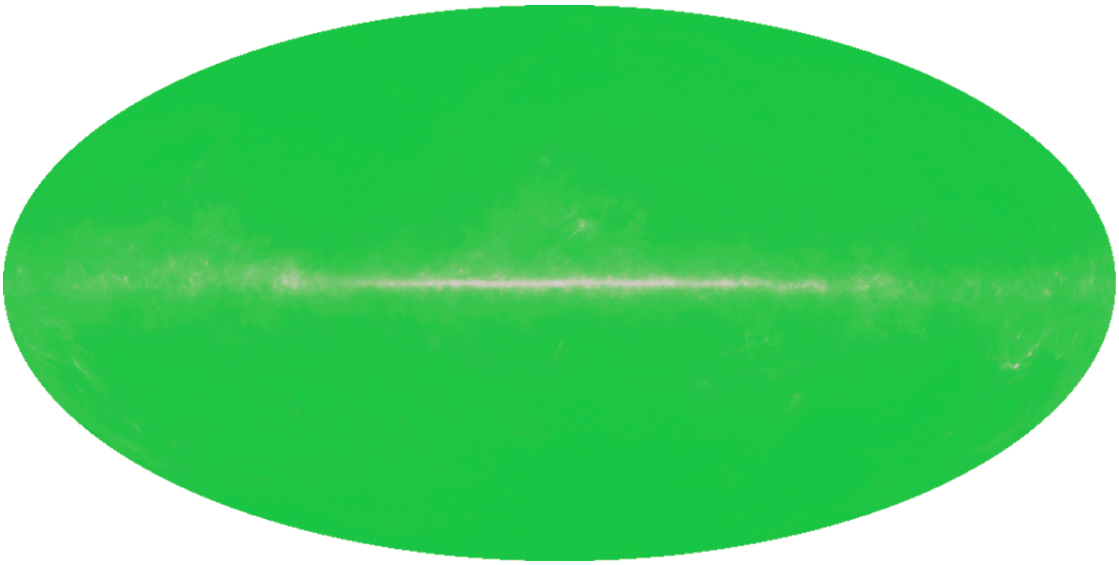

Figure 1.1: Penzias-Wilson temperature sky map at mean temperature of 2.7K. Note that this map is not of temperature anisotropies and the temperature is consistent across the map other than uninteresting noise caused by the Milky Way in the galactic plane.

In 1964, Arno Penzias and Robert Wilson working at Bell Labs, built a horn antenna to detect faint radio waves. In the process of trying to remove all background noise, they discovered that they could not get rid of a persistent 4 GHz signal. Penzias and Wilson were later put in contact with Robert Dicke and David Wilkinson at Princeton who had been working on estimates of the microwave background. Together, they determined that this was the microwave background radiation for which they had been searching. It was well described as a radiating blackbody at 2.7K with a peak radiance of 160.2 GHz with an isotropic temperature distribution [Penzias and Wilson, 1965]. This was strong evidence that we live in a primarily isotropic universe resulting from a Big Bang, at least at the resolutions accessible by the horn antenna.

In 1929, Hubble discovered that the universe is expanding, promoting the Big Bang model to the most acccepted explanation of the origin of the universe. The Friedmann equation relates the rate of the expansion of the universe (namely, the acceleration of the expansion) to the energy density of the universe. In 1998, the Supernova Cosmology Project [Riess et al., 1998] and the High-Z Supernova Search Team observed Type Ia supernovae over

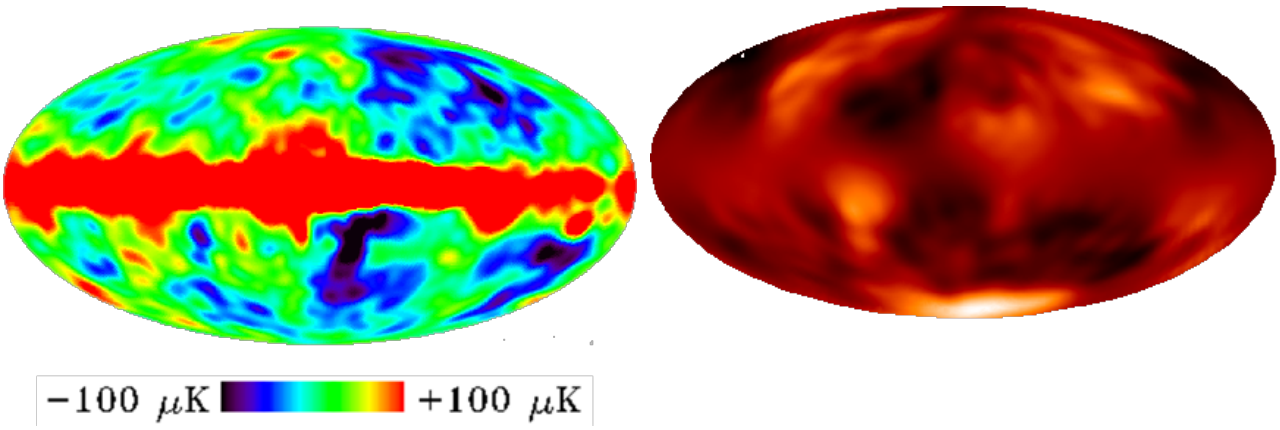

Figure 1.2: COBE temperature sky map and Earth map with same resolution

repeated time-lapsed exposures of the sky to determine their redshift. The fact that these supernovae were farther than expected in a low mass density universe without a cosmological constant was evidence of an accelerating expansion. The negative pressure of dark energy can affect the Friedmann equation to yield the observed acceleration of expansion rate. The simplest model containing such a cosmological constant, known as the Λ-Cold Dark Matter (Λ-CDM) model is a parameterization of the Big Bang model where the universe contains a cosmological constant (Λ) associated with dark energy and cold dark matter and accounts for this expansion of the universe, among other things.

Decades later, the first full-sky detection experiment was run via the Cosmic Background Explorer (COBE) satellite. In 1992, the COBE satellite discovered that not only was the sky isotropic with 2.73K, but that there were temperature fluctuations about this mean temperature on the order of $10^{-4}K$. This was confirmation of the expected anisotropies produced from quantum fluctuations in the early universe. Though the existence of anisotropies became clear with COBE, the angular resolution was limited at around 7° (or $\ell \sim 25$ as a multipole mode) [Smoot, 1999], i.e., COBE was blind to fluctuations on smaller angular scales.

In 2003, the Wilkinson Microwave Anisotropy Probe (WMAP) was launched to measure high resolution (13 arcminutes, or $\ell \sim 800$) CMB with anisotropies at the order of 10^{-4} K. This

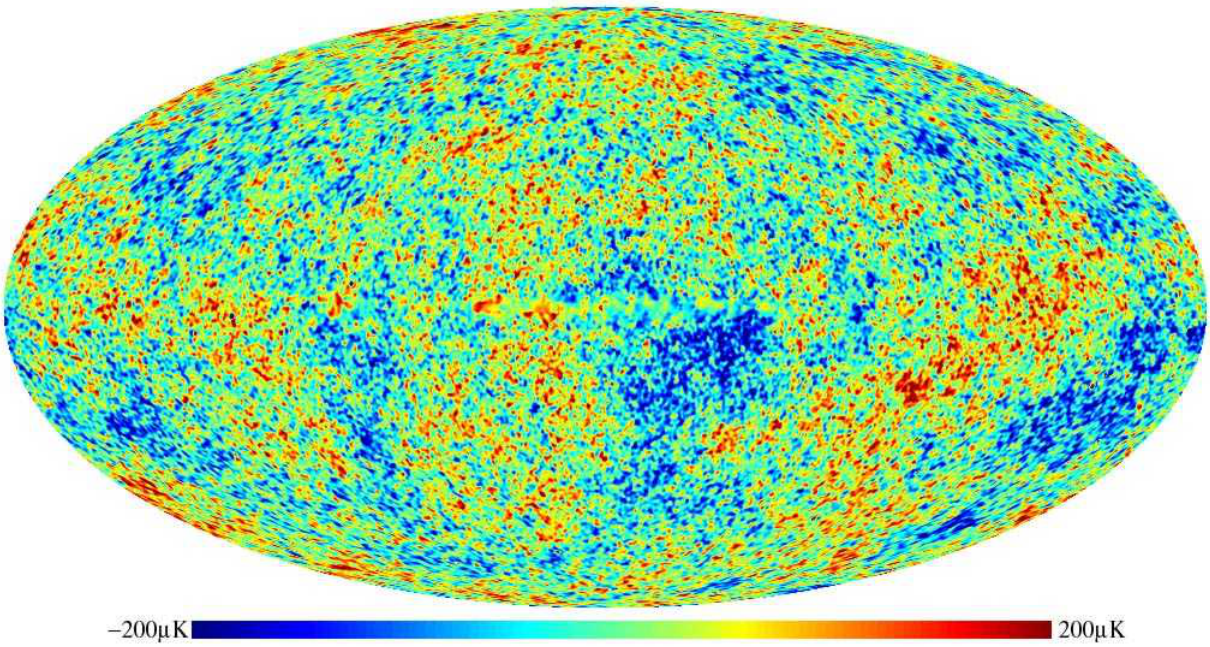

Figure 1.3: WMAP temperature sky map

increased resolution demonstrated a very good fit with the Λ Cold Dark Matter (ΛCDM) model for the Big Bang [Komatsu et al., 2011].

In 2013, another satellite, Planck, was used to make higher resolution measurements of CMB anisotropies on the order of 5 arc minutes ($\ell \sim 2100$). Research using Planck results is still ongoing [Planck Collaboration et al., 2015] and has been used for the majority of the results published in the following works.

The following discussion will focus on how we can use the anisotropies in the CMB to measure attributes of the early universe.

1.1.2 What Can We Learn from the CMB Power Spectrum

The presence of anisotropies in the CMB is makes sense at a basic level by considering quantum temperature fluctuations at the time of the Big Bang. We can use correlations between these temperature fluctuations to measure various attributes of the early universe. If we

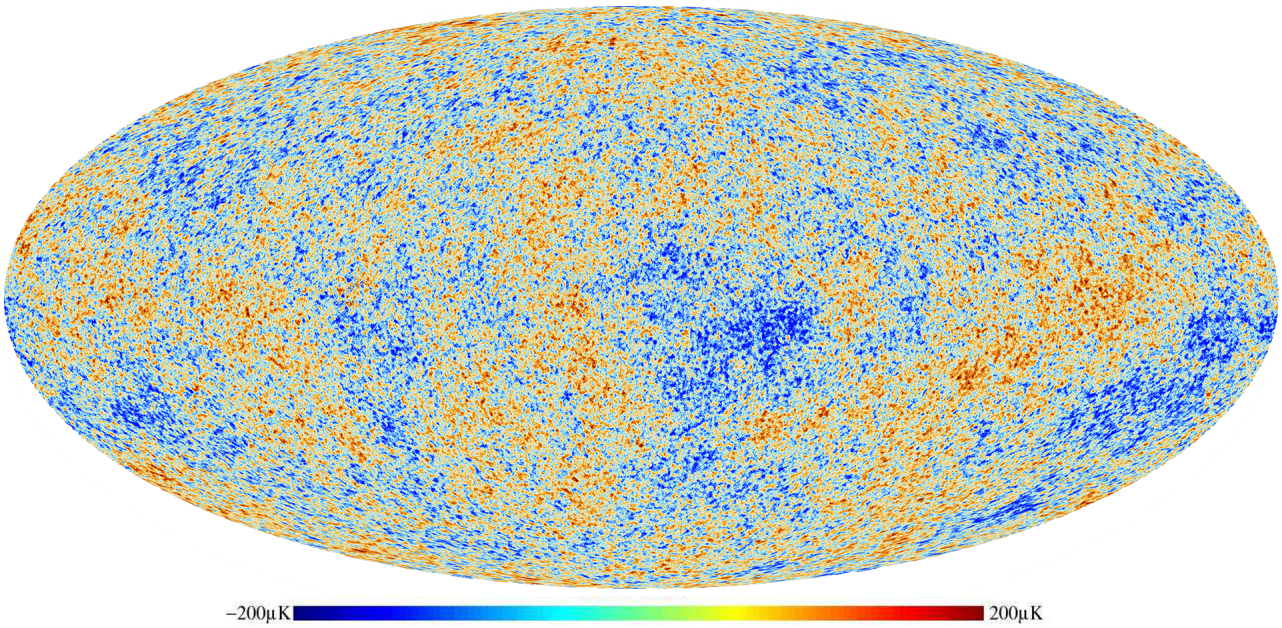

Figure 1.4: Planck temperature sky map

measure the correlation between any two points in the sky and average across those measurements at a given angular scale we get the power spectrum at a given angular separation (or ℓ mode). When we consider all such ℓ modes, we have the power spectrum.

Low ℓ values correspond to larger scale features with more refined features appearing at higher ℓ values. Thus, for the lowest ℓ values, we expect to see information about the initial conditions of the universe.

The irregular distribution of matter in the universe caused baryonic particles to be pulled towards one another due to gravitational attractions while the presence of high energy photons caused matter to be pushed apart (this is called photo pressure). These back and forth interactions led to what is called baryon acoustic oscillations (BAO) (for a review on BAOs, see Bassett and Hlozek [2010]). These oscillations are one of the primary features visible in the power spectrum. Diffusion damping in these oscillations is also visible in the damping behavior at higher ℓ modes in the power spectrum.

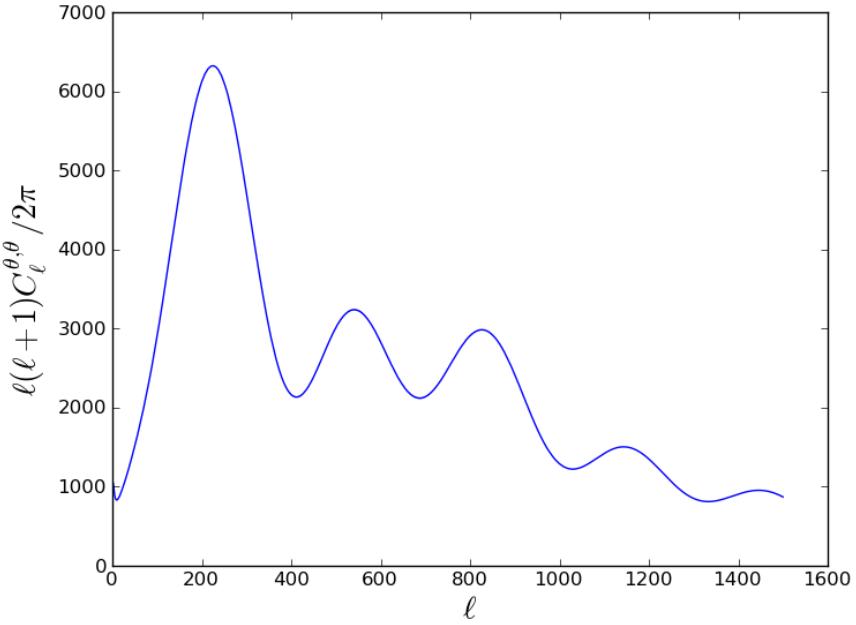

Figure 1.5: Planck power spectrum

The precise position of the first peak in the powers spectrum is very sensitive to the matter composition of the universe, Ω_m. Thus, by measuring the location of the first peak in the power spectrum, we can answer questions about the flatness of the universe. A peak around $\ell \sim 200$ corresponds to a flat universe (more precisely, $\Omega_m = 0.31 \pm 0.01$ according to Planck Collaboration et al. [2015]).

The second peak in the power spectrum (and in general, the ratio of odd to even peak amplitudes) is determined by the baryon density. The baryon density acts as a load to the BAOs, thus an increased baryon density increases the amplitude of BAOs in the compression portion of the cycle, corresponding to the odd peaks. Additionally, since the oscillations are slowed by additional baryonic mass, the peaks will shift to higher ℓ modes with increased baryonic mass. The current best measure for baryonic density is $\Omega_b h^2 = 0.02222 \pm 0.00023$ Planck Collaboration et al. [2015].

To see the effects that can be measured at higher peaks, we consider the progression of

the early universe based on dominant species of matter and energy in given epochs. As the radiation dominated period (earlier on, thus larger time scales relative to the current epoch which correspond to lower ℓ modes) ends and photon density dissipates, gravitational wells become less deep, thus causing oscillations to increase. Thus, we should be able to separate the effects of the dark matter dominated period following radiation domination by considering the higher order peaks. Using the first three peaks, we are able to measure dark matter density.

Additionally, we can consider diffusion effects on higher order peaks we alluded to previously. Namely, since smaller scale oscillations are on the order of the diffusion length scale of photons during recombination, higher order peaks are exponentially damped. Photons at these small scales mix between hot and cold regions of space, thus averaging out and damping oscillations. This provides consistency checks for the standard model of cosmology.

1.2 Inflation

1.2.1 Problems with the CMB

Among the many pieces of information we can extract from the CMB, perhaps the most interesting are the problems with Big Bang cosmology that it highlights. The three largest problems are called the horizon problem, the flatness problem, and the monopole problem.

The horizon problem arises from the fact that causal connections between points in space can only occur at the speed of light. Thus, we should have no correlated patches outside of light cones (namely, scales larger than $\ell \sim 180$, or 1°, should not be correlated with one another). The fact that the sky is nearly isotropic suggests finely tuned initial conditions for our universe.

The flatness problem is a realization that if there universe were to be flat (i.e., local spacetime curvature equal to zero), this would require cosmological parameters to take on an exact value within parameter space (i.e., $\Omega_m = 0.3$) which, assuming all points equally likely, is infinitely improbable. Yet again, we see a fine-tuning issue arising.

The monopole problem is that we would expect to see magnetic monopoles given that Grand Unified Theories (GUT) typically predict them, yet we haven't seen any.

1.2.2 A Solution

One proposed (and the most favored) solution to the above problems is called inflation [Guth, 1981]. Inflationary models are models that cause very rapid expansion shortly after the Big Bang. The amount of expansion that occurs (known as the number of e-folds, N, which is the exponent of e^x used to measure the size of this expansion) is related to measurable quantities like the spectral index (how much density fluctuations can vary with scale in the primordial universe) and the line of sight distance to the surface of last scattering. The expansion is also related to the model used (specifically, to slow roll parameters that will be explained in this section which are dependent on the potential used in a given inflationary model). Using this empirical constraint, we are led to a value of $\sim e^{60}$ for the expansion. The period in which inflation occurs is constrained by this rate of inflation and is thought to have occurred around the time of GUT scales ($10^{15}GeV$ or $10^{-34}s$).

Inflation implies that the universe was much smaller near the time of the Big Bang than if it had been constantly expanding to CMB, thus allowing for causal connections to explain the temperature isotropy seen in the CMB. The flatness problem is solved by introducing a field (the inflaton which is responsible for inflation) whose density does not change its energy density over time, thus resolving a finely tuned initial energy density. Finally, the monopole problem is solved through extreme dilution of monopoles given the expansion of space, thus

accounting for no detections of monopoles.

The most basic model which can achieve the rapid expansion needed for inflationary theories is called slow roll inflation [Brandenberger, 2001]. To see how this model works, consider the Einstein-Hilbert action plus a scalar field,

$$S = \int d^4x\sqrt{|g|}\left(\frac{1}{2}R + \frac{1}{2}\dot{\phi}^2 - V(\phi)\right), \tag{1.1}$$

where $|g| = |\det g_{\mu\nu}|$ and $R = R^{\mu}_{\mu}(g_{\mu\nu})$ the Ricci scalar. Varying the action with respect to the metric

$$\frac{\delta S}{\delta g^{\mu\nu}} = 0 \tag{1.2}$$

$$\implies R_{\mu\nu} - \frac{1}{2}g_{\mu\nu}R = T_{\mu\nu}(\phi). \tag{1.3}$$

where the left hand side depends only on the metric and the right hand side depends only on the scalar field. Using the FRW metric for a flat spacetime curvature,

$$ds^2 = dt^2 - a(t)^2\left(dr^2 + r^2(d\theta^2 + sin^2\theta\, d\phi^2)\right) \tag{1.4}$$

Inserting the metric into the varied action (and using the standard definition $H \equiv \dot{a}/a$), we can solve Eqs. 1.2 to get the Friedman equations

$$H^2 = \frac{1}{3}\left(\frac{1}{2}\dot{\phi}^2 + V(\phi)\right) \tag{1.5}$$

$$\dot{H} = -\frac{1}{2}\dot{\phi}^2. \tag{1.6}$$

The equation of motion is then

$$\ddot{\phi} + 3H\dot{\phi} + \partial_\phi V(\phi) = 0. \tag{1.7}$$

To define inflation (which is just accelerated expansion), we now define

$$\frac{\ddot{a}}{a} = \dot{H} + H^2 = H^2\left(1 + \frac{\dot{H}}{H^2}\right) = H^2(1 - \epsilon_H) \tag{1.8}$$

where ϵ_H is called a slow roll parameter. It's also useful to define the number of e-folds that occur during inflation as

$$dN = -H\,dt \tag{1.9}$$

In the scenario that $\ddot{a}/a > 0$, we must have $0 < \epsilon_H < 1$. To get this condition from Eq. 1.7, we can consider a locally flat potential, $V(\phi)$, thus $\ddot{\phi} \approx 0$, leaving us with

$$\dot{\phi} = -\frac{1}{3H}\partial_\phi V \approx 0 \tag{1.10}$$

Using Eq. 1.5, we have

$$H^2 = \frac{1}{3}V \approx \text{const} \tag{1.11}$$

$$\implies \epsilon_H \approx 0. \tag{1.12}$$

Solving for the scaling factor, we have $a(t) = a_0 e^{H(t-t_0)}$ which produces an exponential expansion. Note that this was done without specifying the potential which could vary from model to model while still yielding inflationary expansion. The potential does, however, need to meet certain conditions to stop inflation from occurring indefinitely.

1.2.3 Signatures

One of the signatures of inflation is the non-Gaussian distribution of temperature perturbations across the sky [Komatsu et al., 2009]. An intuitive explanation goes as follows. Linear curvature perturbations are correlated to temperature fluctuations. If these perturbations are non-Gaussian (i.e., interacting), then the temperature fluctuations will also be non-Gaussian. To see how the curvature perturbations might become non-Gaussian, consider a propagating particle with no interactions. It will behave in a Gaussian manner (spatially). Once you introduce interactions, it becomes non-Gaussian. These non-Gaussianities, however, are small if the interactions are weak since the coupling constants are going to presumably be small since otherwise the interactions involved would have been detected. Thus, with small coupling constants, you'll have small non-Gaussian components. Thus, simple models typically yield very small non-Gaussianities.

We can define curvature pertubations in the sky ($\zeta(x)$) as in terms of Gaussian moments using the usual convention (see e.g., Smidt et al. [2011]),

$$\zeta(x) = \zeta_g(x) + \frac{3}{4} f_{NL} \left[\zeta_g^2(x) - \langle \zeta_g^2(x) \rangle\right] + \frac{9}{25} g_{NL} \zeta_g^3(x) \tag{1.13}$$

where $\zeta_g(x)$ is the purely Gaussian part and f_{NL} and g_{NL} parameterize the first and second non-Gaussian moments. We should note here that we are able to work out the approximate ratio of the non-Gaussian to Gaussian amplitudes as around 10^{-5} (since $f_{NL} \approx 10$ conservatively and the difference in the temperature fluctuations is on the order of 10^{-5}). For general single field models of inflation,

$$f_{NL} = \frac{5}{6} \frac{N''}{(N')^2} \tag{1.14}$$

$$g_{NL} = \frac{25}{34} \frac{N'''}{(N')^3} \tag{1.15}$$

where N is the number of e-folds. These non-Gaussian parameters are commonly used as benchmarks for various inflationary models.

1.3 Measuring Non-Gaussian Modes

The non-Gaussianities predicted by many inflationary models can be quite small and thus need very sensitive measurements. Recall that the power spectrum used earlier is a 2-point correlation function of temperature perturbations across the sky. Correlation functions work well to use in our statistical estimators because of their sensitivity to non-Gaussianities as well as the fact that they have predictions from other effects (e.g., Sunyaev-Zeldovich effect) that can thus be used as filters for measuring weak non-Gaussian signals. In order to measure non-Gaussianities, however, we will need another correlation function (since we can only measure the Gaussian moment using the power spectrum). Note that any non-Gaussian interaction requires a correlation function that contains non-Gaussian information to be measured. That is, any non-trivial interaction (i.e., interactions that are 3-point or more point interactions will contain non-Gaussian components). While it is possible to further generalize our correlation functions beyond 3- and 4-point functions, the analytical calculations used in phenomenological studies for these functions generally become computationally intractable beyond 4-point functions(scaling as number of ell modes raised to the number of points in the correlation function). Additionally, it's important to remember that the interactions we are usually considering when we do studies with correlation functions on the CMB are typically small (otherwise, we would be able to see a visible non-Gaussian component in the CMB temperature fluctuation distribution, but this is not the case).

The 3-point correlation function is called the bispectrum. In the same manner as the power

spectrum, we write the bispectrum as

$$\langle a_{\ell_1 m_1} a_{\ell_2 m_2} a_{\ell_3 m_3} \rangle = \langle B_{\ell_1 \ell_2 \ell_3} \rangle \begin{pmatrix} l_1 & l_2 & l_3 \\ m_1 & m_2 & m_3 \end{pmatrix} \tag{1.16}$$

where the matrix denotes the Wigner-3j symbol and contains geometric constraints induced by the rotational invariance of configuration of the ℓ_i and the other factor on the right hand side (called the reduced bispectrum) contains information related to non-Gaussianity that is defined differently between specific applications.

Similarly, the 4-point correlation function, or the trispectrum, can be written as

$$\langle a_{\ell_1 m_1} a_{\ell_2 m_2} a_{\ell_3 m_3} a_{\ell_4 m_4} \rangle = \sum_{LM} \langle T^{\ell_1 \ell_2}_{\ell_3 \ell_4} \rangle \begin{pmatrix} l_3 & l_4 & L \\ m_3 & m_4 & -M \end{pmatrix} \begin{pmatrix} l_3 & l_4 & L \\ m_3 & m_4 & M \end{pmatrix} \tag{1.17}$$

where the geometric constraints (two Wigner-3j functions corresponding to the two triangle constituents of the quadrilateral made by the 4 points) and reduced trispectrum are defined similarly to the case of the bispectrum. We will see an example below of how the connected part of the reduced trispectrum is computed for second-order non-Gaussianities.

Chapter 2

Constraints on Spatial Variations in the Fine-Structure Constant

2.1 Summary

We use the Cosmic Microwave Background (CMB) temperature anisotropy data from Planck to constrain the spatial fluctuations of the fine-structure constant α at a redshift of 1100. We use a quadratic estimator to measure the four-point correlation function of the CMB temperature anisotropies and extract the angular power spectrum fine-structure constant spatial variations projected along the line of sight at the last scattering surface. At tens of degree angular scales and above, we constrain the fractional rms fluctuations of the fine-structure constant to be $(\delta\alpha/\alpha)_{\rm rms} < 3.4 \times 10^{-3}$ at the 68% confidence level. We find no evidence for a spatially varying α at a redshift of 10^3.

2.2 Introduction

One of the key questions of modern physics concerns the possibility that physical constants vary across space and time in the history of the universe. One possible variation that has received recent attention is that of the fine-structure constant, α. The standard value of α from measurements of the electron magnetic moment anomaly is $\alpha = 1/137.035999074(44)$ [Mohr et al., 2012]. In recent years there has been a great deal of attention given to the possible time and spatial variations of α. From the theory side, such variations are expected from unification [Uzan, 2003] and inflation [Bekenstein, 2002]. From the observational side, contradictory results on the time variability from Webb et al. [1999] and Srianand et al. [2004] regarding absorption line systems have motivated further studies on both the spatial dependence and time variations of α.

Given Thompson scattering of CMB photons, the CMB anisotropy power spectrum probes the value of α at the last-scattering surface at a redshift z of 1100 [Nakashima et al., 2008, Martins et al., 2004, Menegoni et al., 2012, Rocha et al., 2004]. The constraint comes from the variations to the visibility function, or the probability for a photon to scatter at redshift z, at the last scattering surface. This visibility function is a function of α and time variations in α affects the recombination by changing the shape and shifting in time the visibility function, which in turn affect the shape and position of the peaks of the CMB angular power spectrum. The recent Planck analysis (Planck 2014) finds time dependent variations to be constrained to $\Delta\alpha/\alpha = (3.6 \pm 3.7) \times 10^{-3}$ at the 68% confidence level. They additionally constrain dipolar spatial variations to be $\delta\alpha/\alpha = (-2.4 \pm 3.7) \times 10^{-2}$ [Planck Collaboration et al., 2014d].

Moving beyond the time dependence, it is also useful to consider spatial dependence of α. Spatial variations are expected and present in most theoretical models that also introduce a time variation. We highlight two models of interest here. The first involves a scalar particle

coupled to the electromagnetic force leading to loop corrections to α and spatial variations through spontaneous symmetry breaking [Bahcall et al., 2004]. The second involves a cosmological mechanism typical in axion fields where spatial variations in a coupled scalar field arise quantum mechanically during inflation [Sigurdson et al., 2003]. Observationally, an initial claim for spatially varying α exists in the literature with quasar absorption line studies using the Keck telescope and the Very Large Telescope by Webb et. al. [King et al., 2012] in the form of a dipole with a statistical significance of 4.2σ.

While in the recent years CMB has been used to study the global value of α, CMB anisotropies can also be used to study any spatial variations in α at the last scattering surface. If there is some underlying physics responsible for variations in α prior to last scattering one expects α variations to be imprinted on the CMB at the horizon scale and larger. Here we present a first study of such a constraint by making use of the Planck CMB maps. We highlight that this measurement we report here is a constraint on the spatial fluctuations and not the mean or globally-averaged value of α that can be studied from the angular power spectrum. Thus our result we report here will not be directly comparable to quoted α values in the literature from the CMB power spectrum data.

This paper is organized as follows. In Section 2.3, we discuss the effects of small spatial perturbations in α on the CMB temperature maps, their signature in the four-point correlation function (trispectrum), and derive an estimator to measure these effects. In Section 2.6, we present our results and discuss constraints on spatial variations in α as well as future directions.

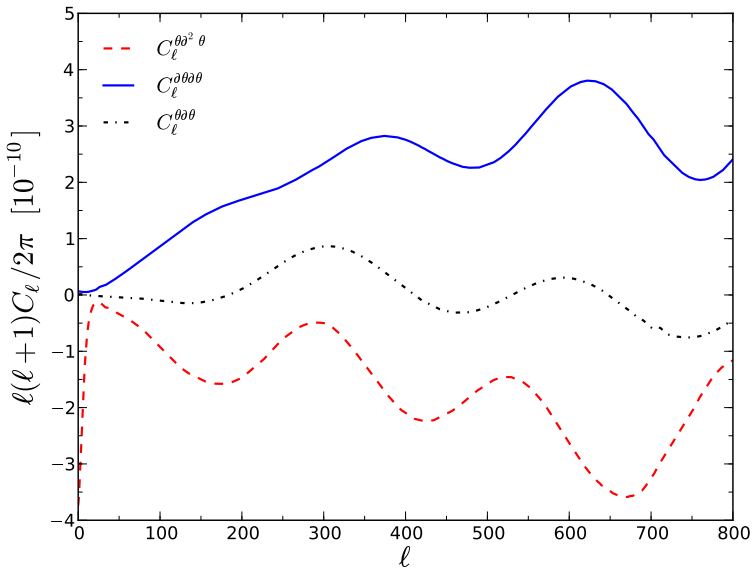

Figure 2.1: Plot of $C_\ell^{\partial\theta\partial\theta}$ (solid; assuming $\delta\alpha/\alpha = 0.08$), $C_\ell^{\theta\partial\theta}$ (dashed dotted; assuming $\delta\alpha/\alpha = 0.01$), and $C_\ell^{\theta\partial^2\theta}$ (dashed; assuming $\delta\alpha/\alpha = 0.01$) derivative power spectra for Planck best fit parameters.

2.3 Effects of Perturbations in Alpha on CMB Temperature Map

The signature of spatial variations in α exist at the four-point function of the CMB anistropies. Thus an optimal estimator that can measure the trispectrum [Hu, 2001], the harmonic or Fourier analogue of the four-point correlation function, induced by α variations is needed to constrain the spatial fluctuations of α. To calculate the observable effects of a spatially-dependent α on the CMB temperature map we follow an approach similar to Ref. [Sigurdson

et al., 2003]. We first perform a spherical harmonics expansion of the temperature field θ:

$$\begin{aligned}
\tilde{\theta}_{\ell m} &\approx \theta_{\ell m} + \int dn\, Y^*_{\ell m} \delta\alpha \frac{\partial \theta}{\partial \alpha} + \frac{1}{2}\int dn\, Y^*_{\ell m} (\delta\alpha)^2 \frac{\partial^2 \theta}{\partial \alpha^2} && (2.1)\\
&= \theta_{\ell m} + \sum_{\ell_1 m_1, \ell_2 m_2} \delta\alpha_{\ell_1 m_1} \left[\left(\frac{\partial \theta}{\partial \alpha} \right)_{\ell_2 m_2} I^{m m_1 m_2}_{\ell \ell_1 \ell_2} \right. && (2.2)\\
&\quad \left. + \frac{1}{2} \left(\frac{\partial^2 \theta}{\partial \alpha^2} \right)_{\ell_2 m_2} \sum_{\ell_3 m_3} \delta\alpha^*_{\ell_3 m_3} J^{m m_1 m_2 m_3}_{\ell \ell_1 \ell_2 \ell_3} \right]
\end{aligned}$$

where the $Y_{\ell m}$ are the spherical harmonics functions and the two integrals I and J are given by

$$\begin{aligned}
I^{m m_1 m_2}_{\ell \ell_1 \ell_2} &= \int dn\, Y^*_{\ell m} Y^*_{\ell_1 m_1} Y^*_{\ell_2 m_2} && (2.3)\\
J^{m m_1 m_2 m_3}_{\ell \ell_1 \ell_2 \ell_3} &= \int dn\, Y^*_{\ell m} Y^*_{\ell_1 m_1} Y^*_{\ell_2 m_2} Y^*_{\ell_3 m_3}\,, && (2.4)
\end{aligned}$$

respectively. In the above $\delta\alpha$ captures the line of sight projected spatial variations in α at the last scattering surface. It modifies the temperature field by coupling to the spatial derivatives of the temperature field θ with respect to the fine-structure constant. It can be shown that, retaining first-order corrections, no signal from $\delta\alpha$ is present in the two-point (power spectrum) or three-point (bispectrum) correlation function of the CMB temperature θ. (This is because we don't see $(\delta\alpha)^2$ terms in correlation functions of θ until we go to the fourth order in θ.) The highest-order corrections related to $\delta\alpha$ is only visible in the CMB at the four-point level of statistics. We thus focus on its effects on the four-point correlation function or, more naturally in terms of the measurement, on the trispectrum.

Furthermore, hereafter we assume these line of sight $\delta\alpha$ fluctuations in the fine-structure constant are Gaussian about the mean value of α at $z = 10^3$. The line of sight projected

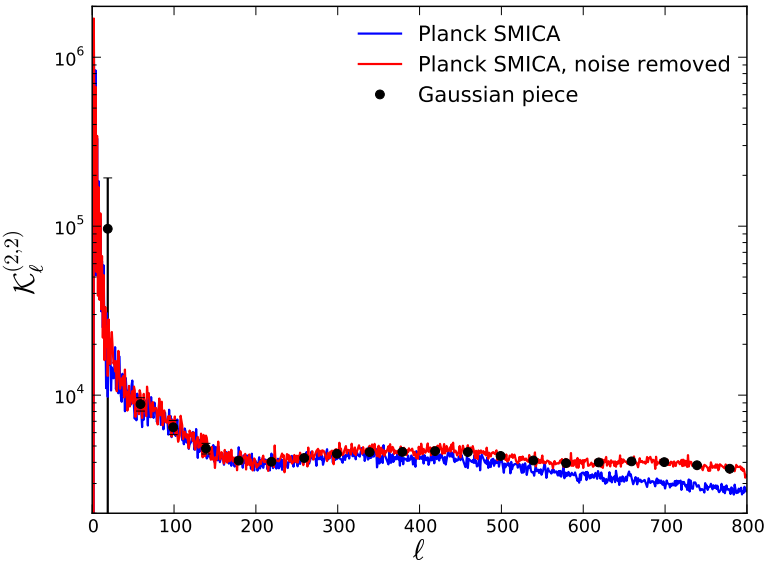

Figure 2.2: The estimator $K_\ell^{(2,2)}$ for Planck SMICA full sky data (blue) and Planck full sky data with noise removed SMICA map (red) compared to that obtained from full sky Gaussian simulations (black).

angular power spectrum can be written as $\langle(\delta\alpha)_{lm}(\delta\alpha)_{l'm'}\rangle = C_l^{\alpha\alpha}\delta_{ll'}\delta_{mm'}$. Our primary goal in this work is a measurement of $C_l^{\alpha\alpha}$ from Planck data. A non-zero measurement of $C_l^{\alpha\alpha}$ will establish the presence of $\delta\alpha$ fluctuations at the last scattering surface and the range in ℓ values over which a non-detection is detected will establish the angular scales on the sky over which $\delta\alpha$ varies from one region of the last scattering surface to another. We assume that the mean value of α, averaged over the last scattering surface, is the standard value and hereafter we fix all other cosmological parameters to the best-fit Planck model [Planck Collaboration et al., 2014d].

2.4 Analytical Effects in the Trispectrum.

The trispectrum can be written as the sum of a Gaussian component and a *connected* term:

$$\langle a_{l_1m_1}a_{l_2m_2}a_{l_3m_3}a_{l_4m_4}\rangle = \langle a_{l_1m_1}a_{l_2m_2}a_{l_3m_3}a_{l_4m_4}\rangle_G + \langle a_{l_1m_1}a_{l_2m_2}a_{l_3m_3}a_{l_4m_4}\rangle_c \,, \tag{2.5}$$

where the $a_{\ell m}$ are the coefficients of the spherical harmonic expansion. In our study the connected term of the Fourier transform, that is, the term remaining after the Gaussian component is subtracted in Eq. 2.5, represents the trispectrum resulting from non-Gaussian correlations due to $\delta\alpha$. The Gaussian and connected pieces can be expanded as [Hu, 2001]

$$\langle a_{l_1m_1}a_{l_2m_2}a_{l_3m_3}a_{l_4m_4}\rangle_G = \sum_{LM}(-1)^M G^{l_3l_4}_{l_1l_2}(L) \begin{pmatrix} l_1 & l_2 & l_3 \\ m_1 & m_2 & m_3 \end{pmatrix} \quad \begin{pmatrix} l_3 & l_4 & L \\ m_3 & m_4 & -M \end{pmatrix},$$

$$\langle a_{l_1m_1}a_{l_2m_2}a_{l_3m_3}a_{l_4m_4}\rangle_c = \sum_{LM}(-1)^M T^{l_3l_4}_{l_1l_2}(L) \begin{pmatrix} l_1 & l_2 & l_3 \\ m_1 & m_2 & m_3 \end{pmatrix} \quad \begin{pmatrix} l_3 & l_4 & L \\ m_3 & m_4 & -M \end{pmatrix},$$

where the quantities in parentheses are the Wigner-3j symbols. The two functions $G^{l_3l_4}_{l_1l_2}(L)$ and $T^{l_3l_4}_{l_1l_2}(L)$ for the Gaussian and connected components, respectively, can be derived analytically. Proceeding from the expansion in Eq. 2.1, after some tedious but straightforward algebra, we arrive at

$$\begin{aligned} G^{\ell_1\ell_2}_{\ell_3\ell_4}(L) = (-1)^{\ell_1+\ell_3}&\sqrt{(2\ell_1+1)(2\ell_3+1)}C_{\ell_1}C_{\ell_3}\delta_{L0}\delta_{\ell_1\ell_2}\delta_{\ell_2\ell_3} \\ &+ (2L+1)C_{\ell_1}C_{\ell_2}\left[(-1)^{\ell_2+\ell_3+L}\delta_{\ell_1\ell_3}\delta_{\ell_2\ell_4} + \delta_{\ell_1\ell_4}\delta_{\ell_2\ell_4}\right] , \end{aligned} \tag{2.6}$$

and

$$T^{\ell_1\ell_2}_{\ell_3\ell_4}(L) = C^{\alpha\alpha}_L F_{\ell_2 L\ell_1} F_{\ell_4 L\ell_3} \times (C^{\theta\partial\theta/\partial\alpha}_{\ell_1} + C^{\theta\partial\theta/\partial\alpha}_{\ell_2})(C^{\theta\partial\theta/\partial\alpha}_{\ell_3} + C^{\theta\partial\theta/\partial\alpha}_{\ell_4})\,, \tag{2.7}$$

where

$$F_{\ell_1\ell_2\ell_3} = \sqrt{\frac{(2\ell_1+1)(2\ell_2+1)(2\ell_2+3)}{4\pi}} \begin{pmatrix} l_1 & l_2 & l_3 \\ 0 & 0 & 0 \end{pmatrix}. \tag{2.8}$$

2.5 Measuring Effects in Planck with the Trispectrum Estimator.

Expanding Eq. 2.7, we have

$$\begin{aligned} T^{\ell_1\ell_2}_{\ell_3\ell_4}(L) &= C^{\alpha\alpha}_L F_{\ell_2 L\ell_1} F_{\ell_4 L\ell_3} \\ &\times (C^{\theta\partial\theta/\partial\alpha}_{\ell_1} C^{\theta\partial\theta/\partial\alpha}_{\ell_3} + C^{\theta\partial\theta/\partial\alpha}_{\ell_1} C^{\theta\partial\theta/\partial\alpha}_{\ell_4} + C^{\theta\partial\theta/\partial\alpha}_{\ell_2} C^{\theta\partial\theta/\partial\alpha}_{\ell_3} + C^{\theta\partial\theta/\partial\alpha}_{\ell_2} C^{\theta\partial\theta/\partial\alpha}_{\ell_4}) \end{aligned} \tag{2.9}$$

For simplicity we rewrite this as

$$T^{(x)\ell_1\ell_2}_{\ell_3\ell_4}(L) = F_{\ell_2 L\ell_1} F_{\ell_4 L\ell_3} F^{(x)}_L \alpha^{(x)}_{\ell_1} \beta^{(x)}_{\ell_2} \gamma^{(x)}_{\ell_3} \delta^{(x)}_{\ell_4} \tag{2.10}$$

where the functions $\alpha_\ell, \beta_\ell, \gamma_\ell, \delta_\ell$ are given in Table 2.1.

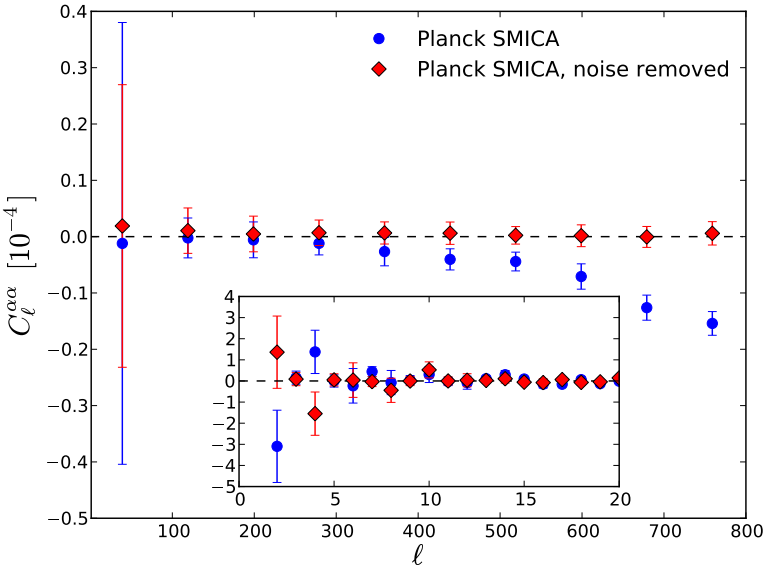

Figure 2.3: Power spectrum of spatial anisotropies of projected fine-structure constant fluctuations at the last scattering surface. The value of $C_\ell^{\alpha\alpha}$ is consistent with zero at 2σ for $\ell < 5$ and at 1σ for the higher multipoles for noise removed maps. The inset shows the low-multipoles range without binning to highlight the fluctuations. We show two sets of measurements here using the Planck SMICA map (blue dots) and the noise-removed SMICA map (red diamonds). The detections at $\ell > 600$ is a result of the noise bias and is removed when using the noise-removed SMICA map. We find no statistically significant detection of α spatial anisotropies once accounting for noise and other instrumental effects in Planck data.

In terms of measuring this trispectrum from the Planck map, we need an estimator. Following Ref. [Smidt et al., 2011], the trispectrum estimator is written as

Table 2.1: Weightings for trispectrum estimator.

x	1	2	3	4
F_L	$C_L^{\alpha\alpha}$	$C_L^{\alpha\alpha}$	$C_L^{\alpha\alpha}$	$C_L^{\alpha\alpha}$
α_{ℓ_1}	$C_{\ell_1}^{\theta\partial\theta/\partial\alpha}$	$C_{\ell_1}^{\theta\partial\theta/\partial\alpha}$	1	1
β_{ℓ_2}	1	1	$C_{\ell_2}^{\theta\partial\theta/\partial\alpha}$	$C_{\ell_2}^{\theta\partial\theta/\partial\alpha}$
γ_{ℓ_3}	$C_{\ell_3}^{\theta\partial\theta/\partial\alpha}$	1	$C_{\ell_3}^{\theta\partial\theta/\partial\alpha}$	1
δ_{ℓ_4}	1	$C_{\ell_4}^{\theta\partial\theta/\partial\alpha}$	1	$C_{\ell_4}^{\theta\partial\theta/\partial\alpha}$

$$\mathcal{K}^{(2,2)}_{\ell,data} = \frac{1}{(2\ell+1)} \sum_m \left[A^{(x)}B^{(x)}\right]_{\ell m} \left[G^{(x)}D^{(x)}\right]_{\ell m} \,, \tag{2.11}$$

where the functions in square parenthesis in (2.11) are:

$$A^{(x)}_{\ell m} \equiv \frac{\alpha^{(x)}_\ell}{\tilde{\mathcal{C}}^\ell} b_\ell a_{\ell m}, \quad B^{(x)}_{\ell m} \equiv \frac{\beta^{(x)}_\ell}{\tilde{\mathcal{C}}^\ell} b_\ell a_{\ell m}, \tag{2.12}$$

$$G^{(x)}_{\ell m} \equiv \frac{\delta^{(x)}_\ell}{\tilde{\mathcal{C}}^\ell} b_\ell a_{\ell m}, \quad D^{(x)}_{\ell m} \equiv \frac{\gamma^{(x)}_\ell}{\tilde{\mathcal{C}}^\ell} b_\ell a_{\ell m} \,, \tag{2.13}$$

where $a_{\ell m}$ are the Fourier coefficients from the Planck map, b_ℓ is the beam transfer function of Planck, and $\tilde{C}^\ell$ is the total power spectrum accounting for noise and beam effects. We write this total power spectrum as $\tilde{C}_\ell = C_\ell b^2_\ell + N_\ell$, with the noise power spectrum given by N_ℓ. In addition to the Planck data map, the team has publicly released b_ℓ and the noise map allowing the noise construction to be done exactly. The above estimator for the trispectrum could simply be understood as the power spectrum of squared temperature map. A second estimator for the trispetrum could be designed by taking the power spectrum of the cubic temperature map correlated with the temperature map, $\mathcal{K}^{(3,1)}_{\ell,data}$. We do not pursue this three-to-one correlation here as we found it to have a lower signal-to-noise ratio than the two-to-two correlations.

The analogous analytical form of the trispectrum estimator can be obtained by expanding

the data estimator with the above weighted maps:

$$\begin{aligned}
\mathcal{K}^{(2,2)}_{\ell,ana} &= \frac{1}{(2\ell+1)}\sum_m \left[A^{(x)}B^{(x)}\right]_{\ell m}\left[G^{(x)}D^{(x)}\right]_{\ell m} \qquad (2.14)\\
&= \frac{1}{(2\ell+1)}\sum_m \left[\frac{\alpha^{(x)}_{\ell_1}}{\tilde{C}_{\ell_1}} b_{\ell_1} a_{\ell_1 m_1} \frac{\beta^{(x)}_{\ell_2}}{\tilde{C}_{\ell_2}} b_{\ell_2} a_{\ell_2 m_2}\right]_{\ell m}\left[\frac{\gamma^{(x)}_{\ell_3}}{\tilde{C}_{\ell_3}} b_{\ell_3} a_{\ell_3 m_3} \frac{\delta^{(x)}_{\ell_4}}{\tilde{C}_{\ell_4}} b_{\ell_4} a_{\ell_4 m_4}\right]_{\ell m}\\
&= \frac{1}{(2\ell+1)}\sum_m \left[\frac{(C^{\theta\partial\theta}_{\ell_1}+C^{\theta\partial\theta}_{\ell_2})(C^{\theta\partial\theta}_{\ell_3}+C^{\theta\partial\theta}_{\ell_4})}{\tilde{C}_{\ell_1}\tilde{C}_{\ell_2}\tilde{C}_{\ell_3}\tilde{C}_{\ell_4}}\left\langle a_{\ell_1 m_1} a_{\ell_2 m_2} a_{\ell_3 m_3} a_{\ell_4 m_4}\right\rangle_c\right]\\
&= \frac{C^{\alpha\alpha}_\ell}{(2\ell+1)^2}\sum_{\ell_i}\frac{F^2_{\ell_2\ell\ell_1}F^2_{\ell_4\ell\ell_3}}{\tilde{C}_{\ell_1}\tilde{C}_{\ell_2}\tilde{C}_{\ell_3}\tilde{C}_{\ell_4}} \times (C^{\theta\partial\theta}_{\ell_1}+C^{\theta\partial\theta}_{\ell_2})^2(C^{\theta\partial\theta}_{\ell_3}+C^{\theta\partial\theta}_{\ell_4})^2\,.
\end{aligned}$$

In the above derivation, we have used the connected piece of the trispectrum and would simply replace this with the Gaussian piece to determine the Gaussian estimator. Note that $\mathcal{K}^{(2,2)}_{\ell,conn} \propto C^{\alpha\alpha}_\ell$ and a direct comparison of $\mathcal{K}^{(2,2)}_{\ell,data}$ to $\mathcal{K}^{(2,2)}_{\ell,ana}$ under the assumption of $C^{\alpha\alpha}_\ell = 1$ in the analytical calculation results in a measurement of $C^{\alpha\alpha}_\ell$ from the data. Before this comparison can be made, we note that $\mathcal{K}^{(2,2)}_{\ell,data}$ in Eq. 2.11 also includes a Gaussian contribution. This has to be removed from the data through numerical simulations and is equivalent to the removal of the noise bias from angular power spectrum measurements from the data.

In the analytical calculations and to define the four α, β, γ and δ functions in the estimator, we used a modified version of `camb` [Lewis et al., 2000]. To handle a varied α in the `camb` (which is used in the derivative power spectrum calculations), we must take into account its effects on the photon visibility function. Replication of these modifications can be achieved by taking into accounts the effects of α upon the Thompson scattering cross section, the hydrogen binding energy, the ionization coefficient, the recombination coefficient, and the recombination rates. (For a detailed discussion of this dependence, see Sigurdson et al. [2003].) Figure 2.1 shows the derivative power spectra $C^{\theta\partial^2\theta}_\ell$, $C^{\partial\theta,\partial\theta}_\ell$, and $C^{\partial\theta\partial\theta}_\ell$. For the analysis presented here the noise power spectrum for Planck was obtained from the publicly available SMICA [Planck Collaboration et al., 2014d] noise map. In addition to beam and

noise effects, corrections to the power spectrum must also be made to account for the masking of the Galactic plane and point sources, among others, with the mask $W(\hat{n})$. The masking results in mode-coupling and can be corrected again through simulations. It was shown by Hivon et al. [2002] that the masking effects on the temperature maps can be removed in the resulting power spectrum by correcting C_ℓ as

$$\tilde{C}_\ell = \sum_{\ell'} M_{\ell\ell'} C_{\ell'} \tag{2.15}$$

where $M_{\ell\ell'}$ is defined as

$$M_{\ell\ell'} = \frac{2\ell'+1}{4\pi} \sum_{\ell''} (2\ell''+1) W_{\ell''} \begin{pmatrix} \ell & \ell' & \ell'' \\ 0 & 0 & 0 \end{pmatrix}^2 \tag{2.16}$$

where W_ℓ is the power spectrum of the mask $W(\mathbf{N})$.

First in order to establish the Gaussian noise bias to the connected two-to-two power spectrum and to account for effects of masking, we created Gaussian simulations using the publicly available `healpix` software [Górski et al., 2005] and Eq.2.11 with $a_{\ell m}$'s obtained from Gaussian realizations of the Planck map, including detector noise as established by the SMICA map. By averaging over the Gaussian simulations, where there are no effects due to $\delta\alpha$ fluctuations, we establish the Gaussian noise term. This is then substracted from the full trispectrum estimator $\mathcal{K}^{(2,2)}_{\ell,data}$ (Eq. 2.11) to obtain only the connected term generated by any non-Gaussian signals in the data, in this case primarily due to $\delta\alpha$ fluctuations.

The full estimator and Gaussian piece are shown in Figure 2.2. After calculating $\mathcal{K}^{(2,2)}_{\ell,ana}$ (Eq. 2.14 analytically assuming $C_\ell^{\alpha\alpha} = 1$, we estimate the power spectrum of $\delta\alpha$ or $C_\ell^{\alpha\alpha}$ by taking the ratio of the Gaussian noise-corrected two-to-two trispectrum measured from CMB data to the analytically derived function. The uncertainties in $C_\ell^{\alpha\alpha}$ from the data are obtained from the set of simulations by allowing for the detector noise to vary to be

consistent with the overall noise power spectrum. We use a total of 250 simulated maps here for the noise-bias correction, to correct for the mask, and for the uncertainty estimates, with the number of simulations restricted by the computational resources to perform this measurement over three weeks. Figure 2.3 shows the angular power spectrum for spatial variations of α, $C_\ell^{\alpha\alpha}$.

2.6 Discussion

As can be seen in Figure 3 the measured $C_\ell^{\alpha\alpha}$ is consistent with zero, showing no evidence for spatial variations of α when projected at the last scattering surface at a redshift of 10^3. The most significant fluctuations are observed for the very low multipoles ($\ell < 5$). However the value of $C_\ell^{\alpha\alpha}$ is always consistent with zero at the 2σ confidence level. We also repeated the analysis described above by keeping the detector noise signal in the original Planck CMB data map to highlight the possible biasing effects due to the noise. The results are shown in Figure 2.3. We find that the noise bias is not affecting substantially the analysis at multipoles less than 300 but is a concern at higher multipoles where noise begins to dominate. From the measured $C_\ell^{\alpha\alpha}$, we obtain the line-of-sight projected rms fluctuation of $\delta\alpha$, properly normalized to value of α today, using $(\delta\alpha/\alpha)^2_{\rm rms} = (1/4\pi)\sum_\ell (2\ell+1) C_\ell^{\alpha\alpha}$. From our measurements, we find $(\delta\alpha/\alpha)_{\rm rms}(z = 10^3) < 6.7\times10^{-3}$ and $< 3.4\times10^{-3}$ for SMICA and SMICA with noise removed, respectively, at the 68% confidence level and over the range of $2 < \ell < 20$, corresponding to angular scales above 10 degrees or super-horizon scales of the CMB. Note that since we are using a 4-point function, we require $\ell \geq 3$, thus variations on scales smaller than 60 (azimuthal) degrees. If we assume $C_\ell^{\alpha\alpha} = A$, a white noise-like power spectrum, then we find $A = (-5.7 \pm 9.4) \times 10^{-5}$ and $(-1.6 \pm 4.8) \times 10^{-6}$ when $2 < \ell < 20$ and $20 < \ell < 500$, respectively. Assuming $C_\ell^{\alpha\alpha}$ is a constant independent of ℓ the reduced χ^2 values of the fit are 1.55 and 0.508 for SMICA and SMICA with noise removed, respectively.

Our overall constraint on the spatial fluctuations of α is from the trispectrum and other non-Gaussian mechanisms that also generate a signal in the trispectrum could easily contaminate or confuse the $\delta\alpha$ variations. The largest signal in the CMB trispectrum is expected from gravitational lensing of CMB photons. The lensing perturbations couple to the spatial gradient of the CMB, $(\vec{\delta\phi}) \cdot \nabla\theta$. In the Fourier domain the two effects are orthogonal to each other and we find that there is effectively no lensing leakage that can mimic the $\delta\alpha$ signal in the trispectrum. Similarly, non-Gaussian signals associated with astrophysical sources, such as galaxies and clusters, peak at smaller angular scales or high multipoles and are independent of the signal we are aiming to measure here. The constraint we are thus reporting here should be robust to most non-Gaussian signals, but apart from lensing and sources, we have not explored all possibilities in the literature.

Our constraint on $(\delta\alpha/\alpha)_{\rm rms}(z = 10^3)$ differs from the constraint placed by the Planck team [Planck Collaboration et al., 2014d] in that it considers variations in multiples strictly above the dipole itself. However, we do note that the magnitude of constraints for low l multipoles in our analysis is consistent with the constraint on the dipole placed by the Planck team. It is about a factor of three better than an indirect constraint one can derive using age-dating of globular clusters in the Galaxy with $\delta\alpha/\alpha$ fluctuation level of 10^{-2} at kilo-parcsec distance scales [Sigurdson et al., 2003]. If the $\delta\alpha$ spatial fluctuations are generated by a light scalar field ϕ coupled to photons with a mass scale m_ϕ around 10^{-28} eV, the resulting $\delta\alpha$ fluctuations will be frozen at the time of last scattering. With cosmological expansion the amplitude of the fluctuations will subsequently decay as inverse of time, t^{-1}. Our upper limit on the $\delta\alpha$ fluctuations, assuming this model description is correct, then would imply $\delta\alpha$ fluctuations at the level of 10^{-7} at $z < 2$. (For some physical intuition, note that larger alpha values in a patch of the sky would mean that there would be more energy required for the ionization of hydrogen atoms, thus free electrons would bind to protons at an earlier time and visible photons would be scattered at an earlier time, thus they would be more energetic (i.e., appear hotter)).While degree-scale fluctuations are yet to constrained,

QSO absorption line studies over the redshift interval $0.2 < z < 3.7$ find a dipole with an amplitude of $\delta\alpha/\alpha_{\ell=1} = (0.97 \pm 0.22) \times 10^{-5}$ [King et al., 2012]. If this dipole traces the smaller scale fluctuations, then our limit from CMB at $z \sim 10^3$ rules out a model involving a light scalar field coupled to photos to generate $\delta\alpha$ fluctuations. In the future we expect another one to two-order of magnitude improvement in $(\delta\alpha/\alpha)_{\rm rms}(z = 10^3)$ constraint with high sensitivity CMB polarization maps and their trispectra with the cosmic variance limit for rms fluctuation detection at the level of 5×10^{-5} with CMB.

2.7 Conclusions

We have used CMB anisotropies as measured by Planck to place limits on the amount by which α my vary spatially. This was done by using an estimator constructed for the trispectrum to determine $C_\ell^{\alpha\alpha}$ from which we are able to obtain information about about the spatial variations in α. Considering the region with maximal signal, we obtained constraints of $(\delta\alpha/\alpha)_{\rm rms} < 3.4 \times 10^{-3}$ at the 1σ confidence level. At a redshift of $z \sim 1100$, we find no sign of spatial variations in the fine-structure constant.

Chapter 3

Measuring the Skewness Parameter with Planck Data

3.1 Introduction

3.1.1 Non-Gaussianities in Inflationary Models

Inflationary models that have non-trivial interactions will inherently contain non-Gaussian components. This is directly analogous to connected diagrams in particle physics. These add additional terms to the exponential term of the propagator which make it non-Gaussian. Some such models include multiple fields and exotic objects such as branes.

By constraining the size of these non-Gaussian components, we can constrain different inflationary models (e.g., the size of the interaction coupling terms in those models) [Komatsu et al., 2009]. Here, we consider the third and fourth order non-Gaussian parameters τ_{NL} and g_{NL}. A previous analysis using WMAP data out to $\ell < 600$ found $-7.4 < g_{NL}/10^5/8.2$ and $-0.6 < \tau_{NL}/10^4 < 3.3$ at the 95% confidence level (C.L.). In this discussion, we will

go through an analysis of the Planck temperature anistropy maps using the kurtosis power spectra to obtain the values of τ_{NL} and g_{NL} jointly.

3.1.2 Detecting Non-Gaussianities with Correlation Functions

In order to measure non-Gaussianities in the CMB, we can turn to the curvature information contained in the CMB

$$a_{\ell m} = 4\pi(-i)^\ell \int \frac{d^3k}{(2\pi)^3}\Phi(k)g_{T\ell}(k)Y_\ell^{m*}(\hat{k}), \tag{3.1}$$

$$\theta(\hat{n}) = \frac{\delta T}{T}(\hat{n}) = \sum_{\ell m} a_{\ell m}Y_\ell^{m*}(\hat{n}) \tag{3.2}$$

where $\Phi(\mathbf{k})$ are the primordial curvature perturbations, $g_{T\ell}$ is the radiation transfer function that gives the angular power spectrum $C_\ell = (2/\pi)\int k^2 dk P_\Phi(k) g_{T\ell}^2(k)$, θ is the field of temperature fluctuations in the CMB, and Y_ℓ^m's are the spherical harmonics.

If the curvature perturbations are entirely Gaussian, then the power spectrum

$$C_\ell = \langle a_{\ell m} a_{\ell m}\rangle = \frac{1}{(2\ell+1)}\sum_m a_{\ell m}a_{\ell m}^* \tag{3.3}$$

will contain all information that can be obtained from correlation functions. Any non-Gaussian components, however, will require an additional correlation function. For that, we turn to the three-point correlation function, or the bispectrum.

As was shown in the introduction, the four-point correlation function can be written as

$$\langle a_{\ell_1 m_1} a_{\ell_2 m_2} a_{\ell_3 m_3} a_{\ell_4 m_4}\rangle = \sum_{LM}(-1)^M \begin{pmatrix} \ell_1 & \ell_2 & L \\ m_1 & m_2 & -M \end{pmatrix} \begin{pmatrix} \ell_3 & \ell_4 & L \\ m_3 & m_4 & M \end{pmatrix} T^{\ell_1\ell_2}_{\ell_3\ell_4}(L) \tag{3.4}$$

The matrices are the Wigner-3j symbols and encode the rotational invariance of correlation functions in the CMB. They are non-zero for configurations where $|\ell_i - \ell_j| \leq \ell_k \leq |\ell_i + \ell_j|$ for any combination of i, j, and k. The trispectrum, $T^{\ell_1\ell_2}_{\ell_3\ell_4}$, can be decomposed into a gaussian and non-Gaussian portion (the connected piece). Since we are looking for the non-Gaussian contribution, we are primarily concerned with the connected trispectrum. The connected trispectrum can be expressed in terms of sums of the products of Wigner-3j and Wigner-6j symbols multiplied by what is called the reduced trispectrum, $t^{\ell_1\ell_2}_{\ell_3\ell_4}$.

To derive the reduced trispectrum, we first assume that the curvature perturbations, ζ, of the universe are generated by inflation in the following way:

$$\Phi(x) = \Phi_G(x) + f_{NL}(\Phi^2_G(x) - \langle\Phi^2_G(x)\rangle) + g_{NL}\Phi^3_G(x) \tag{3.5}$$

where the curvature perturbation and the initial gravitational potential are related by $\Phi = (3/5)\zeta$ and $\tau_{NL} = (6f_{NL}/5)^2$. These fluctuations yield temperature anistropies as:

$$a_{\ell m} = 4\pi(-i)^\ell \int \frac{d^3k}{(2\pi)^3}\Phi(k)g_{T\ell}(k)Y^*_{\ell m}(k) \tag{3.6}$$

where $g_{T\ell}(k)$ is the radiation transfer function of adiabatic fluctuations. Using this relation, we can expand the four-point correlation function and remove the gaussian component (as well as Wigner-3j and Wigner-6j functions) to isolate the reduced trispectrum as

$$\begin{aligned} t^{\ell_1\ell_2}_{\ell_3\ell_4}(L) =& \tau_{NL}\left(\frac{5}{3}\right)^2 \int r_1^2 dr_1 r_2^2 dr_2 F_L(r_1, r_2)\alpha_{\ell_1}(r_1)\beta_{\ell_2}(r_1)\alpha_{\ell_3}(r_2)\beta_{\ell_4}(r_2)h_{\ell_1 L\ell_2}h_{\ell_3 L\ell_4} \\ &+ g_{NL}\int r^2 dr \beta_{\ell_2}(r)\beta_{\ell_4}(r)[\mu_{\ell_1}(r)\beta_{\ell_3}(r) + \beta_{\ell_1}(r)\mu_{\ell_3}(r)]h_{\ell_1 L\ell_2}h_{\ell_3 L\ell_4}, \end{aligned} \tag{3.7}$$

where

$$F_L(r_1, r_2) \equiv \frac{2}{\pi} \int k^2 dk P_\Phi(k) j_L(kr_1) j_L(kr_2), \tag{3.8}$$

$$\alpha_\ell(r) \equiv \frac{2}{\pi} \int k^2 dk (2 f_{NL}) g_{T\ell}(k) j_L(kr), \tag{3.9}$$

$$\beta_\ell(r) \equiv \frac{2}{\pi} \int k^2 dk P_\Phi(k) g_{T\ell}(k) j_L(kr), \tag{3.10}$$

$$\mu_\ell(r) \equiv \frac{2}{\pi} \int k^2 dk g_{NL} g_{T\ell}(k) j_L(kr), \tag{3.11}$$

and

$$h_{\ell_1 L \ell_2} \equiv \sqrt{\frac{(2\ell_1+1)(2\ell_2+1)(2L+1)}{4\pi}} \begin{pmatrix} \ell_1 & \ell_2 & L \\ 0 & 0 & 0 \end{pmatrix}. \tag{3.12}$$

We use publicly available code [Komatsu, 2015a] to calculate α, β, and μ. In the above, $P_\Phi(k) \propto k^{n_s-4}$ is the primordial power spectrum of curvature perturbations, $g_{T\ell}(k)$ is the radiation transfer function that gives the angular power spectrum, $j_\ell(kr)$ are the spherical Bessel functions and r parameterizes the line of sight. These are calculated using publicly available code (ref Komatsu). Plots for fixed values of r available in Fig 3.1.

3.2 Measurements

3.2.1 Optimal Estimators

To calculate $F_L(r_1, r_2)$, we use the algorithm given in Liguori [Liguori et al., 2007] in which we define $\xi = r_2/r_1$, $x = kr_1$ and compress r_1 and r_2 into a single dimension, giving us

$$F_L(\xi) = \frac{2}{\pi} r_1^{1-n_s} \lambda \int dx x^{n_s-2} j_L(x) j_L(tx) \tag{3.13}$$

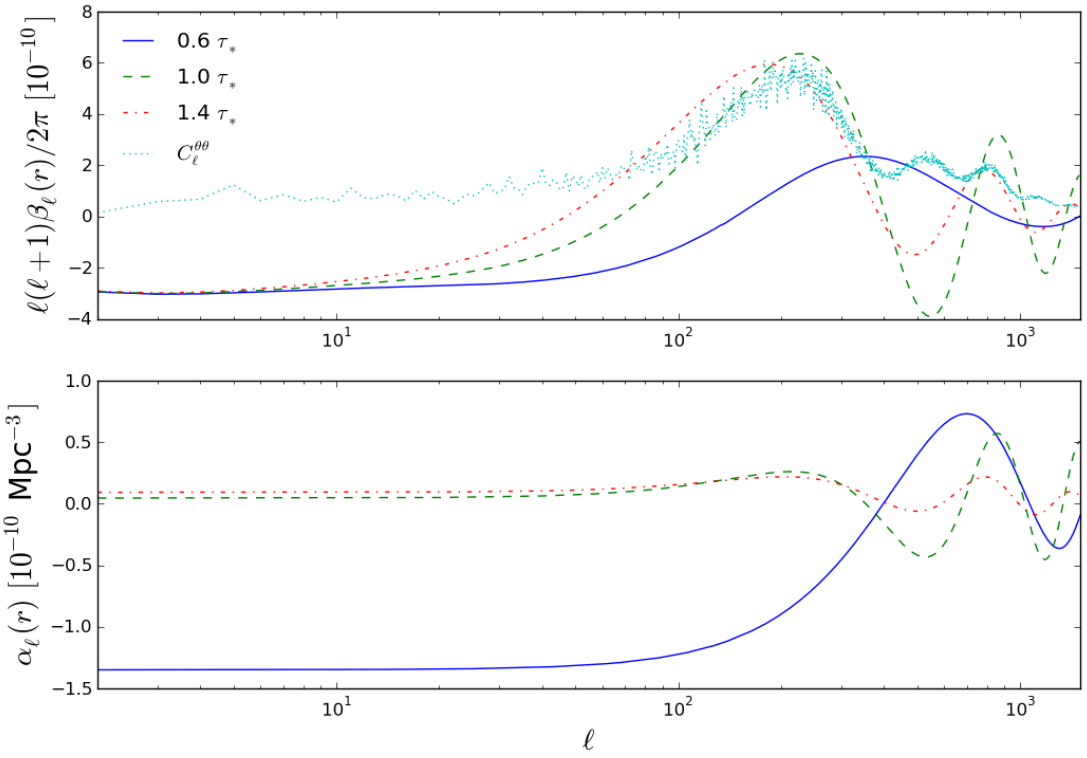

Figure 3.1: Plot of $\alpha_\ell(r)$ and $\beta_\ell(r)$ for various r values where $\tau_* = 235$ Mpc. $C_\ell^{\theta\theta}$ is the power spectrum of the Planck CMB as a reference.

where $\lambda = (3/5)^2(2\pi^2/k_0^3)A_s k_0^{4-n_s}$ and k_0 is the pivot scale set at 0.05Mpc^{-1}.

To calculate the first piece of the trispectrum associated with τ_{NL}, we use the approximation $(5/3)^2 C_L^r \sqrt{C_{\ell_1} C_{\ell_2} C_{\ell_3} C_{\ell_4}}$ given in [Pearson et al., 2012] at $L < 100$. This approximation is valid since the integrand peaks at $r = r_*$ and $C_\ell = \int r^2 dr \alpha_\ell(r)\beta_\ell(r)$. Here r_* is the comoving distance at the surface of last scattering and $C_L^{r_*} = F_L(r_*, r_*)$. When we compare with data, however, we use the exact calculations and utilize an adaptive grid over r.

The ideal estimators for the trispectrum are given by [Munshi et al., 2011]

$$K_L^{(2,2)}(\tau_{NL}, g_{NL}) = \frac{1}{2L+1} \sum_{\ell_1 \ell_2 \ell_3 \ell_4} \frac{1}{2L+1} \frac{t_{\ell_3 \ell_4}^{\ell_1 \ell_2}(L) \hat{T}\ell_3 \ell_4{}^{\ell_1 \ell_2}(L)}{C_{\ell_1} C_{\ell_2} C_{\ell_3} C_{\ell_4}}, \tag{3.14}$$

and

$$K_L^{(3,1)}(\tau_{NL}, g_{NL}) = \frac{1}{2\ell_4+1} \sum_{\ell_1 \ell_2 \ell_3 L} \frac{1}{2L+1} \frac{t_{\ell_3 \ell_4}^{\ell_1 \ell_2}(L) \hat{T}\ell_3 \ell_4{}^{\ell_1 \ell_2}(L)}{C_{\ell_1} C_{\ell_2} C_{\ell_3} C_{\ell_4}}, \tag{3.15}$$

where the reduced bispectrum is evaluated at $\tau_{NL} = 1$ and $g_{NL} = 1$. The estimators $K_L^{(2,2)}$ and $K_L^{(3,1)}$ are parametrized by τ_{NL} and g_{NL}. The function $\hat{T}\ell_3 \ell_4{}^{\ell_1 \ell_2}(L)$ is the full trispectrum from data or simulations.

In this analysis, we let ℓ_i, L values range between 2 and 1000. As can be seen from our definition of the reduced trispectrum, computational times for the estimator will go as ℓ^4 for each value of L (with additional calculation time for the integration over r). To make this calculation more tractable, we employ Monte Carlo integration techniques for the $K_L^{(2,2)}$ estimator. That is, we replaces the sums over ℓ_i with $V/N_{samples} \sum_\ell$ where $\ell = (\ell_1, \ell_2, \ell_3, \ell_4)$ is uniformly sampled over the space $[\ell_{min}, \ell_{max}]^4$ and $V = (\ell_{max} - \ell_{min})^4$. In our $K_L^{(3,1)}$ calculation, we restrict the sum over L to $[2, 20]$ and then ensure that increased L values only negligibly modify the estimator's value. Additionally, we use the triangle inequalities inherent with the WIgner-3j functions to reduce the number of calculations needed. Altogether, our

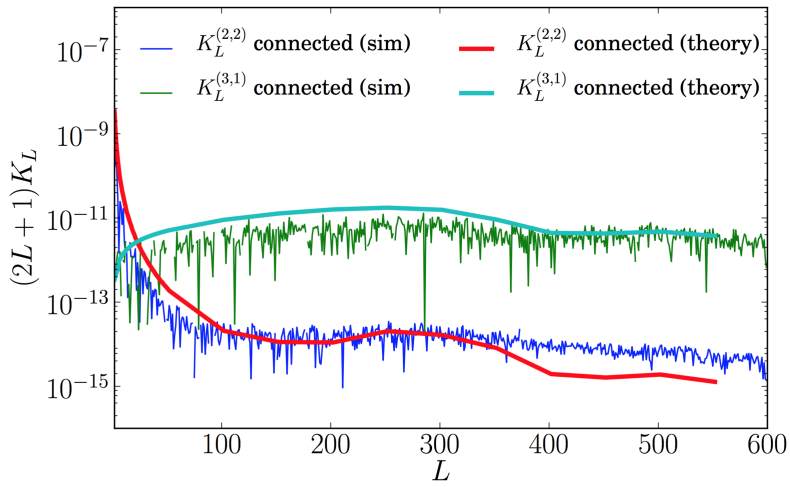

Figure 3.2: The estimator validation using WMAP simulations with $\tau_{NL} = 3600$.

calculation times are on the order of hours which is approximately 1,000 times faster than straight brute-force calculations. Fig. 3.2 shows the estimators for fixed values of τ_{NL} and g_{NL}.

3.2.2 Data Estimators

To create the data estimators, we do the following. First, we create optimally weighted maps,

$$A(r,n) = \sum_{\ell m} \alpha_\ell(r) \frac{a_{\ell m}}{C_\ell} Y_{\ell m}(n), \tag{3.16}$$

$$B(r,n) = \sum_{\ell m} \beta_\ell(r) \frac{a_{\ell m}}{C_\ell} Y_{\ell m}(n), \tag{3.17}$$

where the C_ℓ used in the denominator above contains noise contributions. We correct for a cut sky using a mode coupling matrix as detailed in a later section.

Next, we consider four types of power spectra that we will use to obtain the full $K_L^{(x,x)}$

estimators. Namely,

$$J_\ell^{ABA,B}(r_1,r_2) = \frac{1}{2\ell+1}\sum_m F_L(r_1,r_2)A_{\ell m}(r_1)B_{\ell m}(r_2)A_{\ell m}(r_2)B^*_{\ell m}(r_2), \tag{3.18}$$

$$J_\ell^{AB,AB}(r_1,r_2) = \frac{1}{2\ell+1}\sum_m F_L(r_1,r_2)A_{\ell m}(r_1)B_{\ell m}(r_1)A^*_{\ell m}(r_2)B^*_{\ell m}(r_2), \tag{3.19}$$

$$L_\ell^{ABB,B}(r) = \frac{1}{2\ell+1}\sum_m [ABB]_{\ell m}(r)B^*_{\ell m}(r), \tag{3.20}$$

$$L_\ell^{AB,BB}(r) = \frac{1}{2\ell+1}\sum_m [AB]_{\ell m}(r)[BB]^*_{\ell m}(r). \tag{3.21}$$

When we integrate these power spectra along the line of sight, we get the following:

$$J_\ell^{ABA,B} = \int r_1^2 dr_1 r_2^2 dr_2 J_\ell^{ABA,B}(r_1,r_2); \tag{3.22}$$

$$L_\ell^{ABB,B} = \int r^2 dr L_\ell^{ABB,B}(r); \tag{3.23}$$

$$J_\ell^{AB,AB} = \int r_1^2 dr_1 r_2^2 dr_2 J_\ell^{AB,AB}(r_1,r_2); \tag{3.24}$$

$$L_\ell^{AB,BB} = \int r^2 dr L_\ell^{AB,BB}(r). \tag{3.25}$$

Using these power spectra, we then construct our estimators as

$$K_L^{(2,2)} = \left(\frac{5}{3}\right)^2 J_L^{AB,AB} + 2L_L^{AB,BB} \tag{3.26}$$

$$K_L^{(3,1)} = \left(\frac{5}{3}\right)^2 J_L^{ABA,B} + 2L_L^{ABB,B} \tag{3.27}$$

where the A and B maps used come from data or simulations.

Now that we have these estimators, we use the 143 GHz, 217 GHz, and 143 $\times$ 217 GHz Planck sky maps to obtain the data estimators. Note that for the cross correlated sky map,

the estimators are

$$K_L^{(2,2)}(143\times217) = \left(\frac{5}{3}\right)^2 J_L^{A(143)B(217),A(143)B(217)} + 2L_L^{A(143)B(217),B(143)B(217)} \tag{3.28}$$

$$K_L^{(3,1)}(143\times217) = \left(\frac{5}{3}\right)^2 J_L^{A(143)B(217)A(143),B(217)} + 2L_L^{A(143)B(217)B(143),B(217)}. \tag{3.29}$$

3.2.3 Verifying Simulations

We verify our approximations of the connected trispectra using non-Gaussian CMB signal simulations [Komatsu, 2015b] for WMAP with $n_{side} = 512$, $\ell_{max} = 600$, and cosmological parameters as determined by WMAP-5. To obtain the non-Gaussian signal, namely, $a_{\ell m} = a_{\ell m}^G + f_{NL}a_{\ell m}^{NG}$, we choose $f_{NL} = 50$ (which is equivalent to $\tau_{NL} = 3600$ given the expected relation between f_{NL} and τ_{NL} in our previous assumptions). In these simulations, we use $g_{NL} = 0$ (we do test this assumption in a joint model fit subsequently, however). We then add the WMAP-5 noise to the signal, giving us the temperature map

$$T(n) = \sum_{\ell m} b_\ell p_\ell a_{\ell m} Y_{\ell m}(n) + \frac{\sigma_0}{\sqrt{N(n)}n_{white}(n)} \tag{3.30}$$

where σ_0 (average noise amplitude), $N(n)$ (noise maps), b_ℓ (beam function), and p_ℓ (pixel transfer function) are provided by WMAP. The connected trispectrum estimator can be found by subtracting the Gaussian contribution, namely by using Gaussian realizations of the above temperature map as inputs for the trispectrum estimator,

$$K_L^{conn} = \frac{K_L^{data} - K_L^G}{4!} \tag{3.31}$$

with the extra factor of 4! coming from the different ℓ permutations in the connected piece of the estimator. Fig. 3.2 shows that 100 full-sky simulations are consistent with our approximations.

3.2.4 Accounting for a Cut Sky

With real data, a mask, $W(n)$, is applied to sky maps to mask out things like the galactic plane and known point sources. Taking this into account, our $a_{\ell m}$s become:

$$\begin{aligned}
\tilde{a}_{\ell m} &= \int dn\, M(n) W(n) Y_\ell^{m*}(n), && (3.32)\\
&= \sum_{\ell' m'} a_{\ell' m'} \int dn Y_{\ell'}^{m'}(n) W(n) Y_\ell^{m*}(n), && (3.33)\\
&= \sum_{\ell' m'} a_{\ell' m'} K_{\ell m \ell' m'}[W] && (3.34)
\end{aligned}$$

where $a_{\ell' m'}$ is for the full sky, $M(n)$ is any full sky map, and $K_{\ell m \ell' m'}[W]$ contains all of the cut sky information. Hivon et al. showed that

$$\tilde{C}_\ell = \sum_{\ell'} M_{\ell\ell'} C_{\ell'} \tag{3.35}$$

where $M_{\ell\ell'}$ is a matrix defined as

$$M_{\ell\ell'} = \frac{2\ell'+1}{4\pi} \sum_{\ell''} (2\ell''+1) W_{\ell''} \begin{pmatrix} \ell & \ell' & \ell'' \\ 0 & 0 & 0 \end{pmatrix}^2 . \tag{3.36}$$

In the above, W_ℓ is the power spectrum of the mask, $W(n)$. See Fig. 3.3 for an example. For the same mask, the corrective matrix, $M_{\ell\ell'}$ is displayed in Fig. 3.4

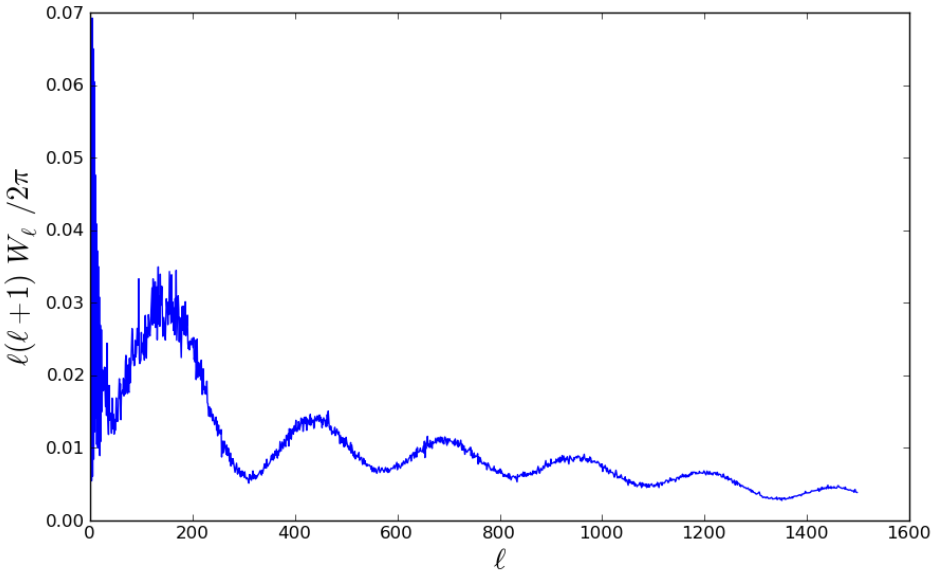

Figure 3.3: Plot of the power spectrum of the Planck mask.

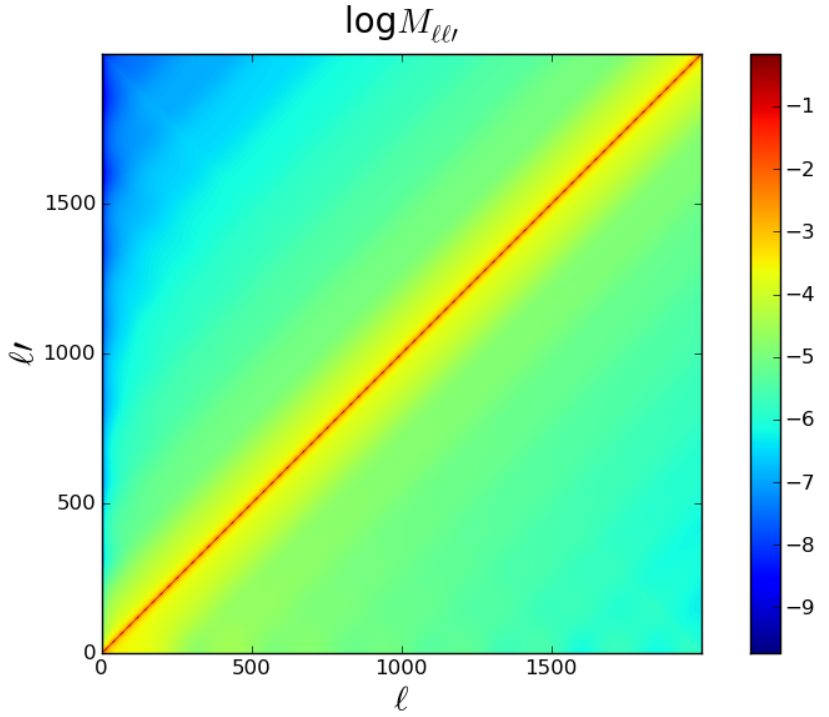

Figure 3.4: Plot of the mode-coupling matrix, $M_{\ell\ell'}$.

3.2.5 Data Analysis

We used Planck 143 GHz and 217 GHz temperature maps for this analysis. Point sources and galactic emissions are removed using a foreground mask. The 217 GHz map needs an extended mask to remove visible light around the galactic plane. The 143 GHz map is convolved with a 7' Gaussian beam and has $45\mu K$ arcmin noise. The noise at 217 GHz is 5' and $60\mu K$ arcmin. As was done by the Planck collaboration in their analysis using similar cleaning techniques [Planck Collaboration et al., 2014b], point sources (PS) and cosmic infrared background (CIB) are included in simulated data. The power spectra for these sources are

$$C_\ell^{PS} = \frac{2\pi}{3000^2} \tag{3.37}$$

and

$$C_\ell^{CIB} = \frac{2\pi}{(\ell(\ell+1))(\ell/3000)^{0.8}} \tag{3.38}$$

respectively. The foreground power spectra are

$$C_\ell^{A\times B} = A_{A\times B}^{PS} C_\ell^{PS} + A_{A\times B}^{CIB} C_\ell^{CIB} \tag{3.39}$$

with parameters given in Table 3.1. Additionally, $10\mu K$ arcmin white noise is added into simulations.

Table 3.1: Power coefficients for point source and cosmic infrared background contributions to power spectra.

	PS	CIB
143	$64\mu K^2$	$4\mu K^2$
217	$57\mu K^2$	$54\mu K^2$
143 × 217	$43\mu K^2$	$14\mu K^2$

The temperature maps for the data are

$$T(n) = \sum_{\ell m} a_{\ell m} b_\ell p_\ell Y_{\ell m}(n) + n(n) \tag{3.40}$$

where n in parentheses is the direction on the sky, the pixel function is at $n_{side} = 2048$, and $n(n)$ is the noise simulation map. We use 100 signal and noise realizations of the FFP6 simulation set of the Planck collaboration [Planck Collaboration et al., 2014c]. To make these realizations, we use the best-fit cosmological parameters from "Planck+WP+highL" [Planck Collaboration et al., 2014a]. Namely,

$$\Omega_b h^2 = 0.022069, \qquad \Omega_c h^2 = 0.12025, \qquad \tau = 0.0927 \tag{3.41}$$

$$n_s = 0.9582, \qquad A_s = 2.21071 \times 10^{-9}, \qquad k_0 = 0.05 Mpc^{-1} \tag{3.42}$$

$$H_0 = 67.15 kms^{-1} Mpc^{-1} \tag{3.43}$$

To calculate the trispectra estimators, we use both Gaussian simulations and data from Planck. For the Gaussian piece of the trispectrum estimator, we average 100 Planck simulations for each of our three temperature maps. We then subtract this Gaussian piece from the full data estimators to isolate the connected piece of the estimator. The estimators are plotted in Fig. 3.5. Note that the Gaussian piece of the estimator is the primary component of the full estimator and is well recreated by Gaussian simulations. We create a covariance matrix, M, from 100 simulations for each frequency combination and the vector $V_b = (V_b^{(2,2)}, V_b^{(3,1)})$, where b is the index of the trispectrum band. For each trispectrum, we choose the five bands $L = [2, 152], [152, 302], [302, 452], [452, 602], [602, 800]$. Note that $\Delta L = 150$ and $L_{cut} = 800$. In order to avoid systematic issues with high L trispectra and to get a higher signal-to-noise ratio, we choose a conservative cut.

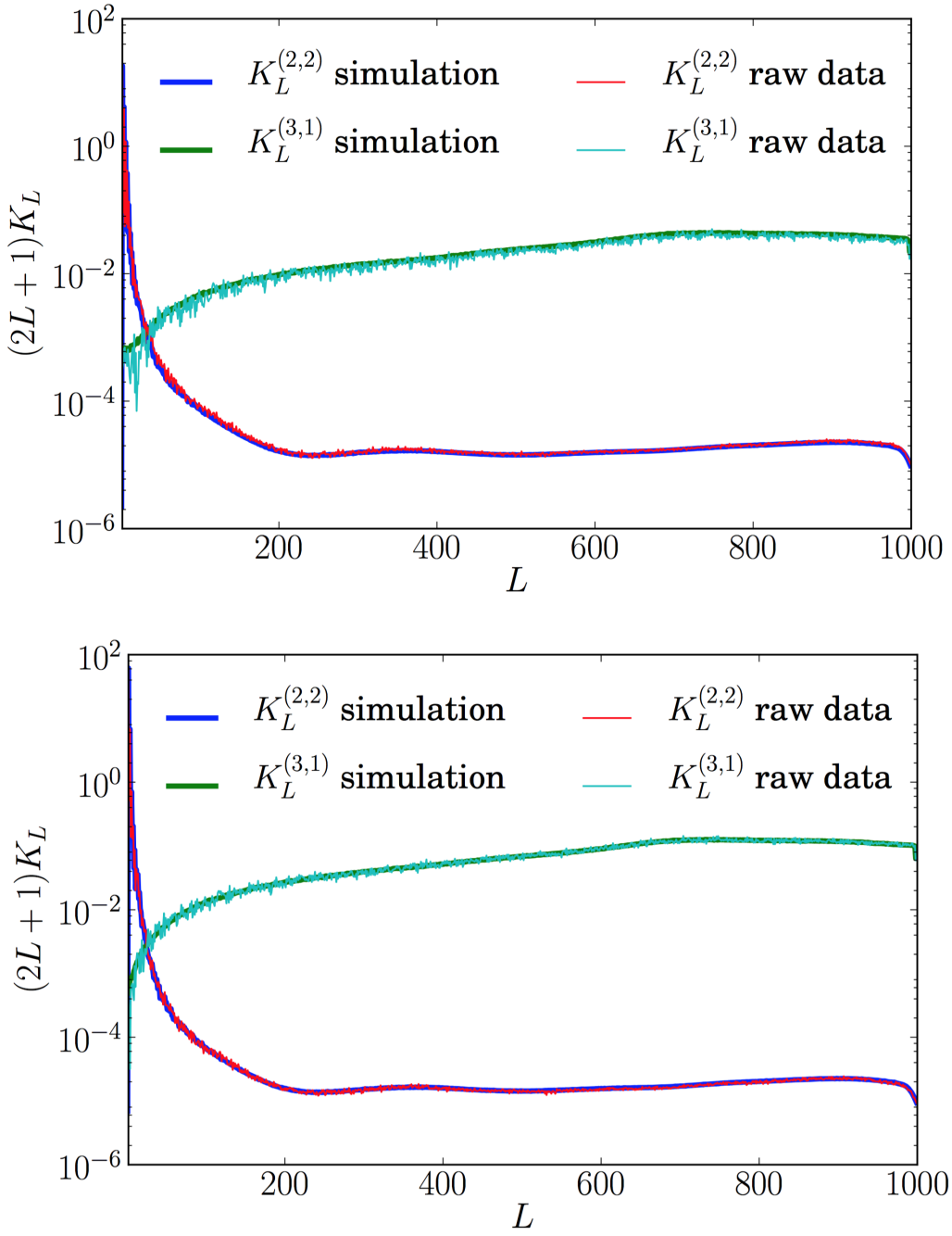

Figure 3.5: Trispectra estimators for the 143 GHz temperature map (top) and 143 $\times$ 217 GHz (bottom). The Gaussian piece is shown by the estimators created from simulations and the full trispectrum from raw data.

We maximize sensitivity by using the binning function,

$$\hat{V}_b = \sum_{L\in b} w_{bL}\hat{S}_L = \frac{\sum_{L\in b} S_L\hat{S}_L/N_L^2}{\sum_{L\in b} S_L^2/N_L^2} \tag{3.44}$$

where $S_L = (2L+1)K_L$ is the fiducial model using $\tau_{NL} = 1$, $g_{NL} = 1$, $N_L = (2L+1)K_L^G$ and $\hat{S}_L = (2L+1)\hat{K}_L$ is the connected trispectrum from simulations or data.

To measure goodness of fit, we use the likelihood function given by

$$\chi^2(\tau_{NL}, g_{NL}) = \sum_{\nu}\sum_{bb'}(V_b^{(\nu)} - \hat{V}_b^{(\nu)})M_{bb'}^{-1,(\nu)}(V_{b'}^{(\nu)} - \hat{V}_{b'}^{(\nu)}) \tag{3.45}$$

where τ_{NL}, g_{NL} are varied to find the best fit and ν is the index of the frequency combination. We then take $\mathcal{O}(10^6)$ samples from Monte Carlo Markov chains with flat priors from $\tau_{NL} \in [-10^6, 10^6]$, $g_{NL} \in [-10^7, 10^7]$. The 217 GHz map retains significant contamination due to CIB after sky cuts, so we do not include this map in our parameter estimation. This yields the results found in Table 3.2. In the last row in Table 3.2, we show the single parameter constraint on g_{NL} using $\tau_{NL} = 0$. For each combination of maps, we find that both τ_{NL} and g_{NL} are consistent with zero. We check different frequency combinations and bin sizes and find consistent results, as shown in Fig. 3.6. From Fig. 3.6, we see that increasing ΔL can result in increased values of g_{NL} which we interpret to mean that the high L range is systematically contaminated by unresolved point sources and non-Gaussian contributions of CIB beyond the mask. Results from Fig. 3.6 are summarized in Table 3.3.

Table 3.2: The constraints for τ_{NL}, g_{NL} with $\Delta L = 150$, $L_{cut} = 800$ for different frequency combinations. The 68% confidence level is given by $\Delta\chi^2 = 2.3$ except for the last row.

Freq. Combination	$\tau_{NL}[\times 10^4]$	$g_{NL}[\times 10^5]$
143×143	-0.6 ± 1.2	-1.9 ± 3.9
143×217	1.9 ± 1.5	-1.0 ± 4.1
$143\times 143 + 143\times 217$	0.3 ± 0.9	-1.2 ± 2.8
$143\times 143 + 143\times 217$	0	-1.3 ± 1.8

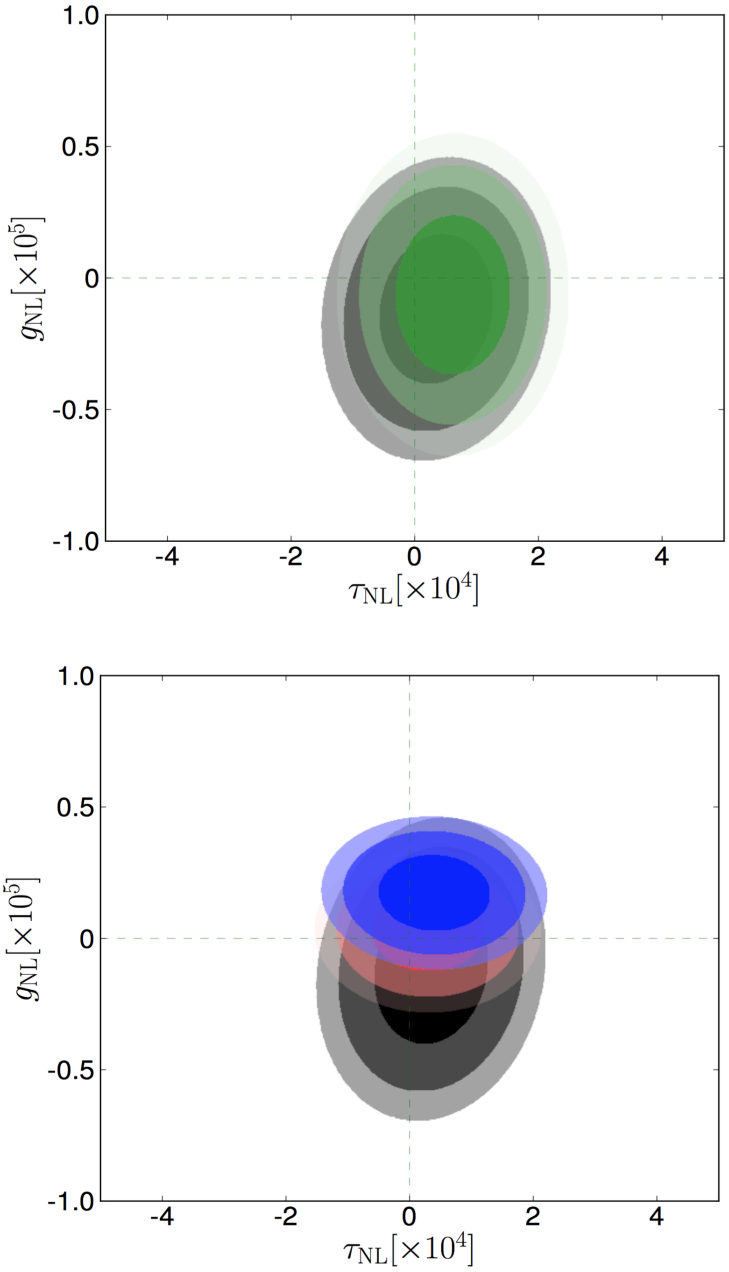

Figure 3.6: The 68%, 95%, and 99% confidence levels for the combination 143×143+143×217 with different bin sizes (top) and L_{cut} (bottom) indicated by the transparency of the contours. For the top, $\Delta L = 150$ is shown in black and $\Delta L = 200$ is shown in green. For both cases, $L_{cut} = 800$. In the bottom, $L_{cut} = 800$ is shown in black, $L_{cut} = 850$ is shown in red, and $L_{cut} = 900$ is shown in blue. In these, $\Delta L = 150$.

Table 3.3: The constraints for τ_{NL}, g_{NL} with different ΔL and L_{cut} for the combination map $143 \times 143 + 143 \times 217$. The 68% confidence level is given by $\Delta\chi^2 = 2.3$.

$143 \times 143 + 143 \times 217$	$\tau_{NL}[\times 10^4]$	$g_{NL}[\times 10^5]$
$[\Delta L = 150, L_{cut} = 800]$	0.3 ± 0.9	-1.2 ± 2.8
$[\Delta L = 150, L_{cut} = 850]$	0.3 ± 0.9	0.3 ± 1.5
$[\Delta L = 150, L_{cut} = 900]$	0.4 ± 0.9	1.7 ± 1.4
$[\Delta L = 200, L_{cut} = 800]$	0.6 ± 0.9	-0.6 ± 3.0

3.3 Conclusion

This analysis is the first joint constraint on τ_{NL}, g_{NL} using Planck data in the kurtosis power spectra that trace square temperature-square temperature and cubic temperature-temperature map power spectra. The Gaussian biases in these estimators are corrected for using simulations. Additionally, we used non-Gaussian simulations to test our pipeline. We found that the best joint estimate of the two parameters is $\tau_{NL} = (0.3 \pm 0.9) \times 10^4$ and $g_{NL} = (-1.2 \pm 2.8) \times 10^5$. If $\tau_{NL} = 0, g_{NL} = (-1.3 \pm 1.8) \times 10^5$.

Bibliography

J. N. Bahcall, C. L. Steinhardt, and D. Schlegel. Does the Fine-Structure Constant Vary with Cosmological Epoch? ApJ, 600:520–543, January 2004. doi: 10.1086/379971.

B. Bassett and R. Hlozek. *Baryon acoustic oscillations*, page 246. Ruiz-Lapuente, P., 2010.

J. D. Bekenstein. Fine-structure constant variability, equivalence principle, and cosmology. Phys. Rev. D, 66(12):123514, December 2002. doi: 10.1103/PhysRevD.66.123514.

R. H. Brandenberger. A Status Review of Inflationary Cosmology. *ArXiv High Energy Physics - Phenomenology e-prints*, January 2001.

K. M. Górski, E. Hivon, A. J. Banday, B. D. Wandelt, F. K. Hansen, M. Reinecke, and M. Bartelmann. HEALPix: A Framework for High-Resolution Discretization and Fast Analysis of Data Distributed on the Sphere. ApJ, 622:759–771, April 2005. doi: 10.1086/427976.

A. H. Guth. Inflationary universe: A possible solution to the horizon and flatness problems. Phys. Rev. D, 23:347–356, January 1981. doi: 10.1103/PhysRevD.23.347.

E. Hivon, K. M. Górski, C. B. Netterfield, B. P. Crill, S. Prunet, and F. Hansen. MASTER of the Cosmic Microwave Background Anisotropy Power Spectrum: A Fast Method for Statistical Analysis of Large and Complex Cosmic Microwave Background Data Sets. ApJ, 567:2–17, March 2002. doi: 10.1086/338126.

W. Hu. Angular trispectrum of the cosmic microwave background. Phys. Rev. D, 64(8):083005, October 2001. doi: 10.1103/PhysRevD.64.083005.

J. A. King, J. K. Webb, M. T. Murphy, V. V. Flambaum, R. F. Carswell, M. B. Bainbridge, M. R. Wilczynska, and F. E. Koch. Spatial variation in the fine-structure constant - new results from VLT/UVES. MNRAS, 422:3370–3414, June 2012. doi: 10.1111/j.1365-2966.2012.20852.x.

E. Komatsu, N. Afshordi, N. Bartolo, D. Baumann, J. R. Bond, E. I. Buchbinder, C. T. Byrnes, X. Chen, D. J. H. Chung, A. Cooray, P. Creminelli, N. Dalal, O. Dore, R. Easther, A. V. Frolov, J. Khoury, W. H. Kinney, L. Kofman, K. Koyama, L. Leblond, J.-L. Lehners, J. E. Lidsey, M. Liguori, E. A. Lim, A. Linde, D. H. Lyth, J. Maldacena, S. Matarrese, L. McAllister, P. McDonald, S. Mukohyama, B. Ovrut, H. V. Peiris, A. Riotto, Y. Rodrigues, M. Sasaki, R. Scoccimarro, D. Seery, A. Sefusatti, K. M. Smith, A. A.

Starobinsky, P. J. Steinhardt, F. Takahashi, M. Tegmark, A. J. Tolley, L. Verde, B. D. Wandelt, D. Wands, S. Weinberg, M. Wyman, A. P. S. Yadav, and M. Zaldarriaga. Non-Gaussianity as a Probe of the Physics of the Primordial Universe and the Astrophysics of the Low Redshift Universe. In *astro2010: The Astronomy and Astrophysics Decadal Survey*, volume 2010 of *Astronomy*, page 158, 2009.

E. Komatsu, K. M. Smith, J. Dunkley, C. L. Bennett, B. Gold, G. Hinshaw, N. Jarosik, D. Larson, M. R. Nolta, L. Page, D. N. Spergel, M. Halpern, R. S. Hill, A. Kogut, M. Limon, S. S. Meyer, N. Odegard, G. S. Tucker, J. L. Weiland, E. Wollack, and E. L. Wright. Seven-year Wilkinson Microwave Anisotropy Probe (WMAP) Observations: Cosmological Interpretation. ApJS, 192:18, February 2011. doi: 10.1088/0067-0049/192/2/18.

Eichiro Komatsu. List of routines, 2015a. URL `http://wwwmpa.mpa-garching.mpg.de/~komatsu/crl/list-of-routines.html`.

Eichiro Komatsu. fnl simulations, 2015b. URL `http://planck.mpa-garching.mpg.de/cmb/fnl-simulations/`.

A. Lewis, A. Challinor, and A. Lasenby. Efficient Computation of Cosmic Microwave Background Anisotropies in Closed Friedmann-Robertson-Walker Models. ApJ, 538:473–476, August 2000. doi: 10.1086/309179.

M. Liguori, A. Yadav, F. K. Hansen, E. Komatsu, S. Matarrese, and B. Wandelt. Temperature and polarization CMB maps from primordial non-Gaussianities of the local type. Phys. Rev. D, 76(10):105016, November 2007. doi: 10.1103/PhysRevD.76.105016.

C. J. A. P. Martins, A. Melchiorri, G. Rocha, R. Trotta, P. P. Avelino, and P. T. P. Viana. WMAP constraints on varying α and the promise of reionization. *Physics Letters B*, 585: 29–34, April 2004. doi: 10.1016/j.physletb.2003.11.080.

E. Menegoni, M. Archidiacono, E. Calabrese, S. Galli, C. J. A. P. Martins, and A. Melchiorri. Fine structure constant and the CMB damping scale. Phys. Rev. D, 85(10):107301, May 2012. doi: 10.1103/PhysRevD.85.107301.

P. J. Mohr, B. N. Taylor, and D. B. Newell. CODATA recommended values of the fundamental physical constants: 2010. *Reviews of Modern Physics*, 84:1527–1605, October 2012. doi: 10.1103/RevModPhys.84.1527.

D. Munshi, A. Heavens, A. Cooray, J. Smidt, P. Coles, and P. Serra. New optimized estimators for the primordial trispectrum. MNRAS, 412:1993–2016, April 2011. doi: 10.1111/j.1365-2966.2010.18035.x.

M. Nakashima, R. Nagata, and J. Yokoyama. Constraints on the Time Variation of the Fine Structure Constant by the 5-Year WMAP Data. *Progress of Theoretical Physics*, 120: 1207–1215, December 2008. doi: 10.1143/PTP.120.1207.

R. Pearson, A. Lewis, and D. Regan. CMB lensing and primordial squeezed non-gaussianity. J. Cosmology Astropart. Phys., 3:011, March 2012. doi: 10.1088/1475-7516/2012/03/011.

A. A. Penzias and R. W. Wilson. Measurement of the flux density of cas a at 4080 mc/s. ApJ, 142:1149, October 1965. doi: 10.1086/148384.

Planck Collaboration, P. A. R. Ade, N. Aghanim, C. Armitage-Caplan, M. Arnaud, M. Ashdown, F. Atrio-Barandela, J. Aumont, C. Baccigalupi, A. J. Banday, and et al. Planck 2013 results. XVI. Cosmological parameters. A&A, 571:A16, November 2014a. doi: 10.1051/0004-6361/201321591.

Planck Collaboration, P. A. R. Ade, N. Aghanim, C. Armitage-Caplan, M. Arnaud, M. Ashdown, F. Atrio-Barandela, J. Aumont, C. Baccigalupi, A. J. Banday, and et al. Planck 2013 results. XVII. Gravitational lensing by large-scale structure. A&A, 571:A17, November 2014b. doi: 10.1051/0004-6361/201321543.

Planck Collaboration, P. A. R. Ade, N. Aghanim, C. Armitage-Caplan, M. Arnaud, M. Ashdown, F. Atrio-Barandela, J. Aumont, C. Baccigalupi, A. J. Banday, and et al. Planck 2013 results. VI. High Frequency Instrument data processing. A&A, 571:A6, November 2014c. doi: 10.1051/0004-6361/201321570.

Planck Collaboration, P. A. R. Ade, N. Aghanim, C. Armitage-Caplan, M. Arnaud, M. Ashdown, F. Atrio-Barandela, J. Aumont, C. Baccigalupi, A. J. Banday, and et al. Planck 2013 results. XXII. Constraints on inflation. A&A, 571:A22, November 2014d. doi: 10.1051/0004-6361/201321569.

Planck Collaboration, R. Adam, P. A. R. Ade, N. Aghanim, Y. Akrami, M. I. R. Alves, M. Arnaud, F. Arroja, J. Aumont, C. Baccigalupi, and et al. Planck 2015 results. I. Overview of products and scientific results. *ArXiv e-prints*, February 2015.

A. G. Riess, A. V. Filippenko, P. Challis, A. Clocchiatti, A. Diercks, P. M. Garnavich, R. L. Gilliland, C. J. Hogan, S. Jha, R. P. Kirshner, B. Leibundgut, M. M. Phillips, D. Reiss, B. P. Schmidt, R. A. Schommer, R. C. Smith, J. Spyromilio, C. Stubbs, N. B. Suntzeff, and J. Tonry. Observational Evidence from Supernovae for an Accelerating Universe and a Cosmological Constant. AJ, 116:1009–1038, September 1998. doi: 10.1086/300499.

G. Rocha, R. Trotta, C. J. A. P. Martins, A. Melchiorri, P. P. Avelino, R. Bean, and P. T. P. Viana. Measuring α in the early Universe: cosmic microwave background polarization, re-ionization and the Fisher matrix analysis. MNRAS, 352:20–38, July 2004. doi: 10.1111/j.1365-2966.2004.07832.x.

K. Sigurdson, A. Kurylov, and M. Kamionkowski. Spatial variation of the fine-structure parameter and the cosmic microwave background. Phys. Rev. D, 68(10):103509, November 2003. doi: 10.1103/PhysRevD.68.103509.

J. Smidt, A. Cooray, A. Amblard, S. Joudaki, D. Munshi, M. G. Santos, and P. Serra. A Constraint on the Integrated Mass Power Spectrum Out to z = 1100 from Lensing of the Cosmic Microwave Background. ApJ, 728:L1, February 2011. doi: 10.1088/2041-8205/728/1/L1.

G. F. Smoot. COBE observations and results. In L. Maiani, F. Melchiorri, and N. Vittorio, editors, *3K cosmology*, volume 476 of *American Institute of Physics Conference Series*, pages 1–10, May 1999. doi: 10.1063/1.59326.

R. Srianand, H. Chand, P. Petitjean, and B. Aracil. Limits on the Time Variation of the Electromagnetic Fine-Structure Constant in the Low Energy Limit from Absorption Lines in the Spectra of Distant Quasars. *Physical Review Letters*, 92(12):121302, March 2004. doi: 10.1103/PhysRevLett.92.121302.

J.-P. Uzan. The fundamental constants and their variation: observational and theoretical status. *Reviews of Modern Physics*, 75:403–455, April 2003. doi: 10.1103/RevModPhys.75.403.

J. K. Webb, V. V. Flambaum, C. W. Churchill, M. J. Drinkwater, and J. D. Barrow. Search for Time Variation of the Fine Structure Constant. *Physical Review Letters*, 82:884–887, February 1999. doi: 10.1103/PhysRevLett.82.884.